

J. metamorphic Geol., 2016, 34, 63–84

doi:10.1111/jmg.12171

Fluid-induced breakdown of monazite in medium-grade metasedimentary rocks of the Pontremoli basement (Northern Apennines, Italy)

D. Lo Pò¹, R. Braga¹, H-J. Massonne², G. Molli³, A. Montanini⁴, T. Theye²

¹ Dipartimento di Scienze Biologiche, Geologiche e Ambientali, Università di Bologna, Piazza di Porta San Donato 1, I-40126, Bologna, Italy

² Institut für Mineralogie und Kristallchemie, Universität Stuttgart, Azenbergstr. 18, D-70174 Stuttgart, Germany

³ Dipartimento di Scienze della Terra, Università di Pisa, Via S. Maria 56, I-56126 Pisa, Italy

⁴ Dipartimento di Fisica e Scienze della Terra, Università di Parma, Parco Area delle Scienze 157a, I-43100 Parma, Italy

Corresponding author: Deborah Lo Pò¹ (deborah.lopo@unibo.it)

Short title: Fluid-induced breakdown of monazite

ABSTRACT

The last (decompression) stages of the metamorphic evolution can modify monazite microstructure and composition, making it difficult to link monazite dates with pressure and temperature conditions. Monazite and its breakdown products under fluid-present conditions were studied in micaschist recovered from the cuttings of the Pontremoli 1 well, Tuscany. Coronitic microstructures around monazite consist of concentric zones of apatite + Th-silicate, allanite, and epidote. Chemistry and microstructure of the monazite grains, which preserve a wide range of chemical dates ranging from Upper Carboniferous to Tertiary times, suggest that this mineral underwent a fluid-mediated coupled dissolution-reprecipitation and crystallization processes. Consideration of the chemical zoning (major and selected trace elements) in garnet, its inclusion mineralogy (including xenotime), monazite breakdown products and phase diagram modelling allow the reaction history among accessory minerals to be linked with the reconstructed *P-T* evolution. The partial dissolution and the replacement by REE-accessory minerals (apatite-allanite-epidote) occurred during a fluid-present decompression at 510 ± 35 °C. These conditions represent the last stage of a metamorphic history consisting of a thermal metamorphic peak at 575 °C and 7 kbar, followed by the peak pressure stage occurring at 520 °C and 8 kbar. An anticlockwise *P-T* path or two clockwise *P-T* loops can fit the above *P-T* constraints. The former path may be related to a context of late-Variscan strike-slip dominated exhumation with minor Tertiary (Alpine-related) reworking and fluid infiltration, while the latter requires an Oligocene-Miocene fluid-present tectono-metamorphic overprint on the Variscan paragenesis.

This article has been accepted for publication and undergone full peer review but has not been through the copyediting, typesetting, pagination and proofreading process, which may lead to differences between this version and the Version of Record. Please cite this article as doi: 10.1111/jmg.12171

This article is protected by copyright. All rights reserved.

KEYWORDS

Monazite geochronology; dissolution-reprecipitation; thermodynamic modelling; medium-grade metamorphism; Northern Apennines.

INTRODUCTION

Monazite is one of the main rare-earth element (REE)-bearing accessory minerals useful for obtaining geochronological information from a wide range of Ca-poor crustal rocks (Williams *et al.*, 2007). In low-grade metamorphic rocks monazite usually occurs as inherited grains or composite crystals made of low-grade neoblasts. During prograde metamorphism of metapelites with typical Ca and Al contents, monazite reacts to form other REE-bearing accessory minerals such as allanite. At Al-silicate-in P - conditions (Al_2SiO_5 polymorphs, cordierite, staurolite) allanite is commonly replaced by new monazite (Wing *et al.*, 2003; Gieré & Sorensen, 2004; Janots *et al.*, 2007, 2008; Goswami-Banerjee & Robyr, 2015). Post-peak metamorphic evolution may result in monazite destabilization, with reaction microstructures (e.g. monazite with coronas in metagranitoids and metapelites) showing its replacement by REE-accessory phases (Finger *et al.*, 1998; Broska *et al.*, 2005) and metapelites (Majka & Budzyń, 2006; Gasser *et al.*, 2012; Massonne, 2014; Balen *et al.*, 2015).

In order to infer the P - T conditions of reactions involving monazite, one approach is to link REE-bearing accessory minerals with the evolution of P - T sensitive phases such as garnet (Vance *et al.*, 2003) through accurate observation of microstructures. Thermodynamically based phase diagrams may then provide thermobaric constraints for the parageneses formed during the metamorphic evolution.

Here we present a study of partially decomposed monazite in garnet-micaschist from the Variscan basement of Northern Apennines beneath Pontremoli (Fig. 1). Monazite breakdown formed coronas of apatite, allanite and epidote by fluid-induced dissolution-reprecipitation and crystallization processes occurring during decompression.

Furthermore, monazite age dating and phase diagram P - T constraints constitute the first attempt to quantify the metamorphic evolution of the Variscan basement beneath the Apennine orogenic belt. The obtained P - T data suggest either a monometamorphic anticlockwise P - T path or a polymetamorphic history due to two clockwise P - T trajectories. Tectonic implications of both suggestions are discussed.

GEOLOGICAL FRAMEWORK

The Northern Apennines are an orogenic belt formed during the collision between the Corsica-Sardinia block and the Adria microplate in the Oligocene-Miocene. In the Northern Apennines, stacked slices of the former Adria continental margin (Tuscan and external foreland units) may be observed below the ocean-derived Ligurian units (Fig. 1). In the inner Northern Apennines, the Tuscan units locally preserve Variscan (i.e. late Palaeozoic) metamorphic rocks below the Mesozoic to Tertiary cover sequences.

The uppermost Tuscan units (Tuscan nappe) show very low grade metamorphic imprint whereas the lowermost ones (Tuscan metamorphic units) were affected by Alpine greenschist facies metamorphism. The Variscan basement is therefore exposed in small fault slices at the base of the Tuscan Nappe, and in the large tectonic windows in the Tuscan Metamorphic units.

Basement rocks occur in several scattered outcrops (i.e Cerreto) but mainly associated with the so-called Mid Tuscan Range, which includes at its northern termination Punta Bianca, Alpi Apuane and Monti Pisani. The Variscan basement was also drilled in the Larderello and

Pontremoli subsurface (Fig. 1). In particular, the Variscan basement in the Pontremoli subsurface has been correlated with the Micaschist Complex of the Larderello geothermal field (Pandeli *et al.*, 2005). This complex underwent low-medium grade metamorphism related to the collisional stage of Variscan orogeny, followed by a post-Variscan peak thermal stage at 285 Ma, an Oligocene-Miocene Alpine greenschist-facies polyphase metamorphism, and, finally, a contact metamorphism associated with the emplacement of Pliocene-Quaternary granites (Franceschini, 1998; Pandeli *et al.*, 2005; Musumeci *et al.*, 2011). Unlike the Micaschist Complex of Larderello, the Variscan basement below Pontremoli was not involved in the contact metamorphism induced by the Neogene igneous activity (Pandeli *et al.*, 2005).

THE SAMPLES

The Pontremoli 1 well intercepted the Variscan basement within a 3059-3520 m depth range (Anelli *et al.*, 1994). Samples AG7 and Pontremoli7 belong to the same core (diameter \approx 10 cm) taken from 3422 m depth (core 7), whereas samples AG8 and Pontremoli8 (core 8) are representative of the basement at 3519-3520 m depth. Analytical procedures are reported in Appendix S1.

Petrography and mineral chemistry

The investigated samples (AG7, Pontremoli7, AG8, Pontremoli8) are of a medium grain size and have a schistose fabric (S_2) with white mica and chlorite wrapping around garnet porphyroblasts (Fig. 2a), which contain inclusions of ilmenite, xenotime, allanite, epidote and pyrite. Pontremoli7 contains a higher volume of garnet (14.2 vol. %) than AG7 (3.7 vol. %). Chlorite and white mica aggregates with a decussate fabric and delineating folds (Fig. 2b) were also observed. Quartz and plagioclase are the other main matrix minerals. Plagioclase hosts white mica and K-feldspar inclusions and shows darker rims than its core in back-scattered electron (BSE) images (Fig. S1). Fractures in garnet are filled with chlorite and white mica. The accessory minerals in Pontremoli7 are ilmenite, rutile, zircon, pyrite, tourmaline, monazite, apatite, thorite, allanite, epidote and xenotime. Ilmenite included in garnet defines an internal foliation (S_1 ; Fig. 2c) whereas euhedral matrix ilmenite is oriented parallel to the main schistosity (S_2). Matrix ilmenite may contain rutile in their cores. Allanite is also present in the matrix and forms aggregates of anhedral grains.

The following mineral data refer to Pontremoli7. Garnet porphyroblasts show a growth zoning with an increase of 13 mol. % and 7 mol. %, respectively, in almandine (Alm) and pyrope (Prp) and a decrease of 12 mol. % in spessartine (Sps) from the inner core to the outermost rim (Figs 3a & 4a,b). The grossular (Grs) + minor andradite (Adr) increase of 8 mol. % from the inner to the outer core, and then decrease to the rim. Typical compositions are $Alm_{72}Sps_{12}Grs(+Adr)_{11}Prp_4$ in the inner core and $Alm_{85}Prp_{11}Grs(+Adr)_3Sps_0$ at the outermost rim (Table 1). Phosphorus is below detection in the inner core, but from the outer core and rimwards increases to a maximum of 180 ppm (Fig. 3b). Garnet also shows a clear zoning profile of Y, Dy, Er and Yb, which are concentrated only in the inner core, but then decrease below detection limit (see above) in both the outer core and the rim (Figs 3b & 4c). In the inner core average values for Y, Dy, Er and Yb are 5500, 1050, 900 and 1000 ppm, respectively.

White mica, occurring as flakes parallel to the main schistosity and as decussate aggregates, is muscovite. There are two types: type I shows Na-rich cores (average Na=0.57 atoms per formula unit (apfu) based on 22 oxygen; average Mg = 0.15 apfu), type II is sometimes relatively Mg-rich at rims (average: Na = 0.29 and Mg = 0.23 apfu; Fig. 3c, d). Type I

Accepted Article

muscovite occurs especially along the schistosity, while type II mainly forms the decussate structures and appears at the maximal bending areas of the late microfolds. Type I muscovite has Si ranging from 6.04 to 6.20 apfu and $\text{Fe}^{2+} + \text{Mg} = 0.19\text{-}0.40$ apfu. Type II muscovite along the schistosity and in aggregates with decussate structure is characterized by $\text{Si} = 6.04\text{-}6.38$ apfu and $\text{Fe}^{2+} + \text{Mg} = 0.19\text{-}0.60$ apfu; while that replacing the garnet rims shows $\text{Si} = 6.06\text{-}6.39$ apfu and $\text{Fe}^{2+} + \text{Mg} = 0.27\text{-}0.64$ apfu (Table 2). X-ray maps of muscovite forming the main schistosity and showing Na-rich cores and Mg-rich rims are displayed in Fig. 4d,e.

Chlorite in different microstructural sites shows limited chemical variations. The $\text{X}_{\text{Fe}} = \text{Fe}^{2+}/(\text{Fe}^{2+} + \text{Mg})$ is 0.60-0.63 for chlorite occurring along the main schistosity, 0.56-0.62 within decussate aggregates, and 0.57-0.63 when surrounding garnet (Table 3).

Plagioclase varies from $\text{Ab}_{89\text{-}92}\text{An}_{8\text{-}10}\text{Or}_0$ in the core to $\text{Ab}_{98\text{-}99}\text{An}_{1\text{-}2}\text{Or}_{0\text{-}2}$ at the rim (Table 4). Plagioclase aggregates near garnet consist of almost pure albite ($\text{Ab}_{99}\text{An}_1\text{Or}_0$).

The microstructural analysis points to a metamorphic evolution in which white mica, chlorite, and ilmenite oriented along the main schistosity (S_2), quartz and plagioclase are interpreted to have re-crystallized during garnet growth. Spessartine rich-garnet inner cores represent the remnant of the prograde stage, while spessartine-poor garnet rims formed during peak temperature. The transition from rutile to ilmenite should predate the garnet growth, because no rutile relicts have been observed in the garnet inner core.

The growth of chlorite and white mica with decussate structure and along fractures in the garnet postdates the formation of the main schistosity. White mica and chlorite replacing garnet rims and the growth of plagioclase rims may be related to a last retrograde metamorphic stage.

Pontremoli7 was studied in more detail because it contains reaction microstructures around relicts of monazite grains (Fig. 2d). The following petrography, mineral data, chemical dating of monazite and thermodynamic modelling refer to Pontremoli7. In this sample irregular xenotime grains with corroded rims occur only in the garnet inner core (Fig. 2e) and epidote surrounding allanite appears in retrogressed garnet rims (Fig. 2f). This sample was, thus, considered to be suitable for an investigation of the reaction history among the REE-bearing minerals.

Coronitic microstructure around monazite

Monazite in Pontremoli7 is surrounded by a complex, polymineralic corona consisting (from the core outwards) of apatite + Th-silicate, allanite and epidote (Fig. 5). This microstructure, which was previously described from amphibolite-facies orthogneisses by Finger *et al.* (1998) and interpreted as the result of monazite-consuming reactions, is associated with every monazite grain in the Pontremoli7 micaschist. The microstructure has a maximum width of 200 μm and may occur at two microstructural sites: (1) in the rock matrix where the microstructure is surrounded by muscovite lamellae (Fig. 5a-c), and (2) in white mica + chlorite aggregates partially replacing garnet (Fig. 5d,e). When the microstructure is elongated, the elongation is parallel to the schistosity (Fig. 5c).

Monazite with a maximum size of 60 μm shows lobate rims in the matrix. The surrounding apatite zone is 10 μm wide, and contains micrometric inclusions of Th-silicate, characterised by its brightness in back-scattered electron (BSE) images and confirmed by qualitative EDS analyses. The apatite zone has clearly-defined protrusions into the surrounding allanite zone. In places apatite grains are within the allanite zone and apatite and Th-silicate can be found also in the allanite zone. Thorite is less abundant in the corona in the retrogressed garnet rim rather than in the matrix corona. The allanite zone has a greater width (up to 100 μm)

when in the garnet rims where only relicts of monazite and apatite are present (Fig. 5d,e). The thickness of the epidote zone ranges from few μm adjacent to matrix ilmenite to 30 μm in white mica matrix. Single epidote grains close to the corona were also observed.

Monazite chemical composition and dating

Only four monazite grains (Mnz01-Mnz04) were found in Pontremoli7. As monazite displays irregular zoning (Fig. 6), several point analyses were acquired in different parts of a single grain in order to fully investigate the intragrain chemical and age variations. Of 75 point analyses only 12 yielded $\text{SiO}_2 < 1$ wt. % and total oxides ranging from 98 to 102 wt. %. Therefore, only these analyses (shown in Fig. 7) were considered to provide meaningful information. The other analyses were rejected because they likely represent mixed analyses because grains are very small (maximum size is 60 μm but the average size is < 10 μm) causing the beam to overlap surrounding (mainly silicate) minerals. Matrix monazite (Mnz01, Mnz02, Mnz04) has $\text{ThO}_2 = 5.9\text{-}9.6$ wt. %, $\text{UO}_2 = 0.3\text{-}0.5$ wt. %, $\text{PbO} = 0.09\text{-}0.13$ wt. %, and $\text{Y}_2\text{O}_3 = 0.01\text{-}0.09$ wt. % (Fig. 8a,b). Monazite in the retrogressed garnet rim (Mnz03) has a different chemistry, with lower ThO_2 (1.33-2.22 wt. %), UO_2 bdl, and PbO (up to 0.02 wt. %) and higher Y_2O_3 contents (0.31-0.32 wt. %).

Chemical dating of monazite followed the approach of Montel *et al.* (1996), using the microprobe analytical setting presented by Massonne (2014). EMP chemical dating of monazite with the above mentioned analytical conditions has successfully provided ages in other studies for both Palaeozoic and Tertiary monazite (Massonne *et al.*, 2007; Langone *et al.*, 2011; Liu *et al.*, 2011; Massonne, 2014). The two analyses of the monazite occurring in the garnet rim, with UO_2 below the detection limit and high Y_2O_3 values (Fig. 8b), were not considered for the age calculation. The dates (in the sense of Williams *et al.*, 2006) derived from the remaining 10 analyses consist of nine older dates ranging from 311.5 ± 6.5 Ma to 250.4 ± 6.5 Ma and a single young date of 19.2 ± 0.3 (statistical 1σ error) Ma, having a low ThO_2 content (Fig. 8c; Table 5). The relative probability plot and histogram of the monazite dates (Fig. 8d) reveals that the two oldest dates yielded a weighted mean of 309.9 ± 5.1 Ma (weighted mean on the two analyses with a 2σ error of the mean; $\text{MSWD} = 0.66$), five dates are the most frequent ones with an average of 292.9 ± 3.0 Ma ($\text{MSWD} = 0.36$) and the dates 281.3 ± 5.7 Ma, 250.4 ± 6.5 Ma and 19.2 ± 0.3 Ma provide single peaks.

GEO-THERMOBAROMETRY

Phase diagram calculation

Thermodynamic modelling was used to derive a P - T path for samples Pontremoli7 + AG7 and, in particular, the thermobaric conditions during the growth of chemically different garnet domains in this rock. Because of limited drill core material it was not possible to undertake a conventional XRF analysis to be used in the calculation of the isochemical phase diagrams. Moreover, the presence of zoned garnet required the calculation of different bulk compositions (as in Fiannacca *et al.*, 2012) to take into account possible modifications of the effective bulk compositions (Stüwe, 1997), for instance, due to the concentration of elements such as Mn in the garnet core. For these reasons, three different bulk compositions were calculated to model different stages of the metamorphic evolution. An initial, unfractionated bulk-rock chemistry was calculated by combining mineral modes and average mineral compositions (bulk1), a bulk composition after the removal of the garnet core (bulk2) and the whole garnet (bulk3). Calculation procedures of the bulk rock chemistry and input parameters for phase diagrams

calculations are respectively reported in Appendices S2 and S3. Calculated bulk-rock compositions are in Table 6.

Prograde path towards peak conditions (bulk1)

In the P - T pseudosection for bulk1, muscovite is stable throughout the entire P - T range (Fig. 9). Chlorite and Na-Ca white mica (Pg in Fig. 9) disappear above 550°C at 3 kbar and 600°C at 6-7 kbar, being replaced by staurolite and plagioclase. The garnet-in curve is located at 400°C - 5 kbar and 450°C - 3 kbar. Biotite occurs above 510 °C (at 7 kbar). The plagioclase-in curve is located below 7 kbar. Zoisite disappears above 450°C-480 °C and below 400 °C. Ilmenite is replaced by rutile only at 350-500 °C. Titanite-bearing P - T fields occur below 450 °C. Isopleths for molar fractions of the garnet inner core $\text{Alm}_{72}\text{Sp}_{12}\text{Grs}(+\text{Adr})_{11}\text{Prp}_4$ intersect in a small area at 530 °C and 5.5 kbar in the paragenetic field chlorite + muscovite + plagioclase + ilmenite + garnet + paragonite + quartz. However, paragonite was not observed probably because it broke down during the decompression. The temperature derived from these isopleths is 130°C higher than the temperature of the garnet-in curve. This may be due to reaction overstepping, to an imperfect correspondence of the maximum-Mn analysis of garnet and the true Mn-content of the garnet innermost core, or a deviation of calculated and true Mn content for bulk1. The presence of calculated ilmenite is in agreement with the observed ilmenite inclusions in garnet. The calculated Si in potassic white mica is 6.12-6.14 apfu around 530 °C and 5.5 kbar, which is within the observed Si range of type I muscovite (Si=6.04-6.20 apfu). The calculated XFe of chlorite is 0.56-0.69 at such P - T conditions, which closely matches observed 0.56-0.62 XFe of chlorite along the schistosity. Garnet isopleths corresponding to the outer core composition do not intersect. This may be due to a fractionation effect of some elements into the garnet inner core. The fractionation effect was then considered for the following pseudosections.

Peak P - T conditions (bulk2)

In the bulk2 P - T pseudosection the topology is different compared to that of bulk1 (Fig. 10). Muscovite appears again in the entire P - T range, but chlorite is stable up to 525 °C at 2 kbar and 600 °C at 8 kbar. Na-Ca-white mica disappears above 525°C at 2 kbar and 600°C at 5 kbar. The staurolite-in curve runs from 530°C at 3 kbar to 600°C at 7 kbar. Ilmenite replaces rutile above 450°C. The P - T field of garnet is reduced compared to that of bulk1. The geothermobarometry with garnet isopleths defines P - T conditions around 575°C and 6.5 kbar for the rim compositions $\text{Alm}_{83-85}\text{Prp}_{7-11}\text{Grs}(+\text{Adr})_{3-8}$. These conditions meet with the paragenetic fields containing muscovite, paragonite, chlorite, garnet, ilmenite, biotite and quartz. However, paragonite and biotite were not observed likely because of their breakdown in the decompression retrograde stage. The P - T isopleth for the maximum Si content in type I muscovite (6.20 apfu) intersects the garnet compositional isopleths at 570 °C and 6.5 kbar.

Retrograde path (bulk3)

Since the garnet rim was in equilibrium with the Na-rich core (type I) of the muscovite along the main schistosity, the rims of muscovite (type II) and chlorite in decussate aggregates should postdate the garnet growth. Muscovite is stable in the entire P - T range (Fig. 11) whereas Na-white mica breaks down above 525°C at 2 kbar and 600 °C at 5 kbar. Chlorite occurs up to 600 °C at 8 kbar. Biotite forms at ≥ 500 °C. Staurolite occurs around 550-600 °C and above 3 kbar. Albite appears in the range 300-500 °C below 8 kbar (500°C). At higher temperatures (520-600 °C), this pressure limit is about 5 kbar. The isopleths of the maximum Si in type II muscovite

(6.38 apfu) and of the minimum XFe ratio in chlorite (0.56), both forming the decussate aggregates, intersect at 520 °C and 8 kbar. These conditions are in the paragenetic field muscovite + chlorite + ilmenite + paragonite + quartz. The observed paragenesis muscovite + chlorite + albite + ilmenite + quartz ± paragonite allows the retrograde path to be constrained passing through 475-520 °C and 2-7 kbar. The calculated Si of muscovite in the fields corresponding to the observed last retrograde paragenesis (6.10-6.35 apfu) is close to the Si in the observed type II muscovite (total range= 6.04-6.38 apfu).

DISCUSSION

Fluid-induced breakdown of monazite and implications for age interpretation

Textural evidence indicates that the U-Th-bearing monazite broke down and a corona consisting of successive zones of apatite, allanite and epidote formed. The inclusions of Th-silicate into the apatite zone indicate monazite replacement by apatite, rather than just apatite growth around monazite. The apatite protrusions into the allanite zone suggest that allanite replaced also the original monazite. The epidote filling the fractures in the allanite zone within the retrogressed garnet rim (Fig. 5e) suggests that it grew around the zone and did not replace monazite. In addition, the monazite shows irregular zoning for Ce, Th, and Y (Fig. 6). Both microstructural and compositional features of monazite suggest a mechanism of fluid-mediated coupled dissolution-precipitation (Williams *et al.*, 2011; Upadhyay & Pruseth, 2012). Fluid-aided alteration can partially reset the oldest monazite age even at temperatures below the “closure temperature” for Th in monazite, as experimentally shown by Williams *et al.* (2011). These authors performed an experimental investigation in which a 350 Ma monazite underwent compositional change under amphibolite-facies conditions in the presence of fluids. Altered domains exhibiting irregular and patchy compositional zonation were developed, with lower Th, U and Pb contents than in the unaltered domains. The altered domains are located also in the monazite cores. Dating of the altered monazite provided scattered and less precise younger “ages” (Williams *et al.*, 2011).

The wide compositional difference between the U-Th-bearing and U-Th-poor monazite in this study suggests a similar mechanism of a fluid-aided alteration process. The formation of the allanite corona implies the reaction of monazite with fluids delivering Ca, Fe, Mg, Si and Y. Dissolution of monazite by Ca-bearing fluid plays a key role in promoting allanite formation (Budzyń *et al.*, 2011).

Fluid-induced alteration of monazite results in a partial resetting of the monazite age (Williams *et al.*, 2011), and a wide spread of dates is also seen in this study. This partial resetting resulted in intermediate dates (range 281-250 Ma) between 293 Ma and 19 Ma obtained in this work. Despite the uncertainty regarding chemical dating of young monazite, the youngest recorded age of 19 Ma may thus be considered as a clear indicator of a Tertiary event. This value represents a maximum age for the fluid-rock interaction, which thus occurred during the Alpine orogenesis.

Another feature suggesting a fluid-aided dissolution-precipitation process is the pseudomorphic shape of the apatite-allanite zones around monazite in the matrix (e.g. Mnz1 and Mnz2 of Fig. 7), confirming that altered monazite, apatite and allanite formed after replacing the original grain of monazite (Upadhyay & Pruseth, 2012). The mixed dates provided by the residual monazite in those coronas corroborate the alteration mechanism interpretation.

It is worthy of note that the monazite with very low Th, U and Pb is located in the garnet retrogressed rim. The maximum extent of the alteration process occurred in this microstructural

Accepted Article

site causing the loss of U and/or Pb in monazite with a total reset of the older ages. The retrogression of garnet could have provided important elements (Ca, Fe, Mg) that enhanced a nearly complete monazite and apatite substitution in favour of allanite. The wider allanite zone (and the smaller monazite and apatite relicts) in the retrogressed garnet rim compared to the coronitic microstructures in the matrix confirms that garnet breakdown played a role in the extent of the allanite crystallization. An alternative interpretation for the monazite crystallization in the retrogressed garnet rim lies in a different mechanism rather than dissolution-reprecipitation: the U-Th-poor monazite could have formed by low-temperature fluid-related crystallization. In this case the matrix U-Th-bearing monazite (MnzI) and the U-Th-poor monazite (MnzII) grew at different times by different mechanisms and not because one was reset more than the other. Some chemical and microstructural data support this interpretation: (i) the high-Y content in monazite from the retrogressed garnet rim suggest that garnet breakdown was involved in the monazite formation; (ii) the minor modal abundance of thorite in the corona in the retrogressed garnet rim rather than in the matrix corona may indicate that the original monazite (pre-corona growth) had a low-Th content which is typical of low-grade monazite (Rasmussen & Muhling, 2009). The Mnz02 rim providing the single 19 Ma age could be another occurrence of the younger monazite generation (MnzII). In the BSE image of Fig. 7, the point dated 19 Ma is located in a bright edge on irregular resorbed monazite, suggesting that it must have formed during or after monazite resorption.

The products of the monazite breakdown (apatite, allanite, epidote) have lower density than the reactant (monazite; Deer *et al.*, 1992), indicating that monazite was consumed during decompression and concomitant infiltration of fluids. Thus, we propose that the monazite breakdown occurred along with that of garnet to chlorite + muscovite that was associated with the retrograde decompression trajectory from 520°C, 8 kbar to 475-520 °C, 2-7 kbar (Fig. 11). Since uncertainties in the peak pressure estimates must be considered, we follow the suggestion by Massonne (2013) who proposed 2 σ -errors in the respective range of 10 and 5% of the corresponding pressure and temperature estimates. For this reason we infer that the partial breakdown of monazite and the development of the apatite, allanite and epidote zones occurred in the range 475-545 °C and 8-2 kbar during exhumation. Interestingly, the *P-T* estimates of several amphibolite-facies metagranitoids with apatite-allanite-epidote coronas around monazite reported by Finger *et al.* (1998) lie in the range of 500–600 °C and 4-7 kbar. In addition, other works report that the breakdown of monazite and the formation of corresponding coronas is associated with fluid infiltration during a retrograde stage (Broska & Siman, 1998; Ondrejka *et al.*, 2012; Upadhyay & Pruseth, 2012).

Follow-up work on the Pontremoli rocks might include dating xenotime, which should give a reliable age for the prograde evolution, and the matrix zircon, which is most likely of detrital origin thus providing a maximum constraint on the metamorphic age.

***P-T* estimates of the metamorphic evolution**

The calculated *P-T* constraints by pseudosections match the observed phase compositions and mineral assemblages; a few discrepancies between observed and calculated parageneses can be explained by the complete retrogression of some phases. For example, paragonite is always present in the calculated *P-T* pseudosections, but it has not been observed. A possible explanation is that paragonite is present in the studied rocks as intergrowths with muscovite or paragonite was replaced by muscovite and albite during the final decompression stage (Fig. 11).

The garnet inner core compositional isopleths indicate 530 ± 25 °C and 5.5 ± 0.6 kbar, which is compatible with the $562^\circ\text{C} \pm 30^\circ\text{C}$ obtained from the Y-Al-garnet (YAG)-xenotime thermometer calibrated by Pyle & Spear (2000).

The peak temperature is 575 ± 30 °C at 6.5 ± 0.7 kbar, constrained by the garnet rim and Na-rich muscovite core (type I) compositions. The lack of xenotime in the garnet rim reflects its complete consumption that occurred during garnet growth above 5-6 kbar, as theoretically predicted by Spear & Pyle (2010). The xenotime breakdown also explains the Y zoning in garnet (Fig. 4b) where maximum Y content (5500 ppm in the garnet inner core) decreases to below the detection limit in the garnet outer core and in the rim because all Y was already sequestered by garnet cores during xenotime breakdown. The low Y in monazite (< 1300 ppm) excludes this mineral from being the source of Y for the garnet inner core. In contrast, the Y and the HREE concentrations in garnet are controlled by consumption of xenotime that shows resorption features and occurs exclusively in the garnet inner core. Since monazite appearance is at about 600 °C (Wing *et al.*, 2003; Gieré & Sorensen, 2004; Janots *et al.*, 2007, 2008; Goswami-Banerjee & Robyr, 2015), we argue that Th-bearing monazite grew coeval with the garnet rim (575 ± 30 °C). Thus the monazite ages of 310 and 293 Ma (excluding mixed dates) indicate that the Pontremoli micaschist likely attained peak conditions in the Variscan or late-Variscan.

The pressure peak (8.0 ± 0.8 kbar at 520 °C) is retrieved by Mg-rich type II muscovite and chlorite within decussate aggregates. Type I muscovite was re-oriented and relatively Mg-rich rims formed during the peak pressure stage. The lack of biotite at the *P-T* peak may be due to its complete retrogression to chlorite and muscovite during the retrograde evolution. The retrograde evolution ended at 475-520 °C and 2-7 kbar during a static stage, constrained by the development of the late retrograde assemblage muscovite + chlorite + albite + ilmenite + quartz ± paragonite (Fig. 12).

***P-T* paths**

A monometamorphic anticlockwise path (Fig. 13a) or two different clockwise loops (Fig. 13b,c), separated by a mostly unpreserved retrograde stage, can fit the above *P-T* constraints. The anticlockwise trajectory would start at 530°C and 5.5 kbar, reaching peak conditions at 575 °C at ~7 kbar, followed by a pressure increase after garnet growth at decreasing temperatures. A tectonic exhumation responsible for the nearly isothermal decompression at 475-520 °C characterizes the late retrograde stage (Fig. 13a). An alternative hypothesis implies an intermediate retrograde stage between two metamorphic cycles, i.e. after the temperature peak (Fig. 13b) and before the maximum pressure (Fig. 13c). The occurrence of K-feldspar inclusions within plagioclase (Fig. S1) indicates that a former ternary feldspar, formed near the temperature peak, exsolved a K-rich component from the plagioclase during a possible intermediate retrograde cooling stage.

The polycyclic *P-T* path hypothesis is supported by the Tertiary monazite age that would imply an Oligocene-Miocene metamorphic overprint on the Variscan Pontremoli basement. Polymetamorphic rocks are known to occur in the Variscan orogenic belt. Massonne (2014) reconstructed a two-cycle orogenic history in the Migmatite Gneiss Zone of the Jubrique Unit of the Betic Cordillera (southern Spain). Eclogite-facies gneiss from the Southern Armorican Massif (France) with an apparent anticlockwise *P-T* path have been shown to be polycyclic rocks characterized by two difficult-to-resolve *P-T* trajectories (Godard, 2009). Thus these basement rocks underwent two separate cycles separated by a retrogression stage that led to the development of replacement microstructures during the cooling.

Tectonic implications

The pre-Oligocene metamorphic record in the Variscan basement of the Northern Apennines is known from the Larderello subsurface basement (Bertini *et al.*, 1994; Pandeli *et al.*, 2005) and the Cerreto micaschist-amphibolite outcrops (Molli *et al.*, 2002). In the Larderello and Cerreto basements, only retrograde segments of Variscan P - T paths (Bertini *et al.*, 1994; Molli *et al.*, 2002) were recognized, but no information on the prograde metamorphic stages. The reconstruction of a complete P - T loop for the Pontremoli basement, which has been traditionally inferred to be Variscan (Pandeli *et al.*, 2005), provides important insights into its late- to post-Variscan evolution.

In spite of the limited age data set and the wide age spread obtained, we can propose some geochronological interpretations. The oldest age indicates monazite growth at 312 Ma in agreement with the Variscan metamorphic event recorded in mafic amphibolites from the Cerreto Pass (312 and 328 Ma; Molli *et al.*, 2002). The early Permian monazite age of 293 Ma, which dates the peak metamorphism, is close to the 285-275 Ma Rb/Sr bulk rock age obtained for the Variscan basement outcropping in the Monti Pisani (Borsi *et al.*, 1967; Ferrara & Tonarini, 1985), and with the 285 ± 11 Ma Rb/Sr age for a muscovite associated with andalusite in a Larderello micaschist (Del Moro *et al.*, 1982), interpreted as a late Variscan thermal perturbations. The early Permian igneous activity accompanying the collapse of the Variscan orogen would be responsible for this thermal anomaly. This activity is demonstrated by large intrusions at different crustal levels of mantle-derived magmas in the Western-Central Alps, Corsica and Apennine basement, ranging from low- (Hermann *et al.*, 2001; Montanini & Tribuzio, 2001; Peressini *et al.*, 2007) to mid-crustal (Braga *et al.*, 2001; Monjoie *et al.*, 2005), and shallow depths (Tribuzio *et al.*, 2009; Renna *et al.*, 2013).

The two contrasting P - T paths proposed above can be explained by the following scenarios (Fig. 13). The first (monometamorphic anticlockwise P - T - t path; Fig. 13a) has an anticlockwise segment followed by a nearly isothermal decompression, which is linked to the activity of a regional scale shear zone accommodating transpressive (anticlockwise: T_{\max} before P_{\max}) to transtensive (near isothermal decompression) deformation (McCann *et al.*, 2006). This tectonic setting predates the Late Triassic to Jurassic extension associated with the opening of the Western Tethys (Marroni *et al.*, 1998; Mohn *et al.*, 2012; Piccardo *et al.*, 2014). The final decompression evolution at 475-520 °C and 2-7 kbar may be consistent with a Mesozoic rifting setting. Transpressive tectonics has been documented in the Mid-Permian in the Southern Alps (Cadel, 1986; Cadel *et al.*, 1996; Deroin & Bonin, 2003), while several Variscan basement complexes record extensional deformation from uppermost Carboniferous to Mid Triassic times (e.g. 280-210 Ma in the Ivrea lower crust; Brodie *et al.*, 1989). This model is consistent with regional evolution, suggesting the importance of intracontinental strike-slip tectonics (Arthaud & Matte, 1977; Doglioni 1984; Massari, 1986; Ziegler, 1986; Handy & Zingg, 1991; Schmid, 1993; Matte, 2001), and with the depositional history of Upper Carboniferous-Mid Triassic sediments of the Tuscan Domain (Rau, 1990; Molli, 2002).

The second (polymetamorphic clockwise P - T paths; Fig. 13b,c) proposes a polycyclic evolution. The first metamorphic cycle involved a prograde formation of the garnet over the period given by the oldest monazite ages of 310 – 293 Ma, followed by retrogression. The second cycle was the Alpine metamorphic overprint, which resulted in a prograde evolution during which peak pressure conditions were reached, followed by fluid infiltration during exhumation yielding monazite partial dissolution and resetting or crystallization. This reworking probably occurred within the 27-11 Ma age range defined by Ar-Ar dating of white mica from

the Alpi Apuane phyllites (Kligfield *et al.*, 1986). These ages record the underplating of the Adria microplate below the Corsica-Sardinia block and subsequent early exhumation of the Adria continental margin (Fellin *et al.*, 2007; Molli, 2008). In this model the tectonic loading during the thickening stages may explain the pressure peak of the *P-T* path for the Pontremoli micaschist. According to various authors (Theye *et al.*, 1997; Giorgetti *et al.*, 1998; Jolivet *et al.*, 1998; Molli *et al.*, 2000) nearby Verrucano siliciclastic metasedimentary rocks attained similar peak pressures (8-12 kbar) in the Miocene supporting this loading, which was possibly followed by rapid exhumation due to crustal extension leading to the opening of the Tyrrhenian Sea (Carmignani & Kligfield, 1990). Alpine metamorphism has previously been documented in the Variscan basement of the Northern Apennines (Monti Pisani and Punta Bianca; Lo Pò & Braga, 2014; Lo Pò *et al.*, 2015 and references therein) where chloritoid-bearing phyllites record a metamorphic peak at 475°C and 9-10 kbar. However, the correlation between the Alpine evolution recorded in the Pontremoli sample and in other Alpine metamorphic units of Northern Apennine is still difficult to constrain.

CONCLUSIONS

1. The breakdown sequence monazite(I) → monazite(II) → apatite + Th-silicate → allanite → epidote occurred during decompression at 2-7 kbar at a temperature of 510 ± 35°C, as a result of fluid-mediated coupled dissolution-reprecipitation and crystallization during exhumation. Fluids released during the reactions involving garnet breakdown reacted with the late-Variscan monazite causing U depletion, a partial resetting of the monazite age and growth of low-Th monazite.
2. The Pontremoli micaschist experienced the following *P-T* conditions: 530°C and 5.5 kbar during the prograde path, a metamorphic peak temperature at 575°C and 7 kbar. The peak pressure is 8 kbar at 520°C followed by a retrogression at 475-520 °C and 2-7 kbar.
3. Two alternative tectonic interpretations can be proposed for the above *P-T* constraints: The first interpretation is for a single anticlockwise *P-T* path related to Permian–Mid Triassic strike-slip development. In this model, an early transpression stage was followed by a later transtension before the opening of the Western Tethys and a fluid-infiltration and static overprint during Alpine orogenesis. The second interpretation is for two separate clockwise *P-T* loops. The Pontremoli micaschist experienced a late-Variscan metamorphism (293 Ma), followed by a retrograde stage that is recorded by the K-feldspar exsolutions in plagioclase. The subsequent attainment of the peak pressure followed by a second retrograde stage occurred during the Alpine orogenesis, when a fluid-rock interaction event induced the breakdown of monazite.

ACKNOWLEDGEMENTS

We thank G. Gasparotto for assistance in SEM-EDX work and E. Dinelli for XRF analyses at University of Bologna. G. Godard is also acknowledged for his suggestions. Reviews by J. Majka, I. Fitzsimons were constructive and helped to improve the paper. D. Robinson is thanked for additional comments and editorial handling. The University of Bologna financed this study (Marco Polo to D.L.P. and RFO to R.B.).

REFERENCES

- Anelli, L., Gorza, M., Pieri, M. & Riva, M., 1994. Surface well data in the Northern Apennines (Italy). *Memorie della Società Geologica Italiana*, **48**, 461-471.
- Anthony, J.W., Bideaux, R.A., Bladh, K.W. & Nichols M.C., 2011. Handbook of Mineralogy, Mineralogical Society of America, Chantilly, VA 20151 – 1110, USA. <http://www.handbookofmineralogy.org/>
- Arthaud, F. & Matte, Ph., 1977. Late-Paleozoic strike-slip faulting in southern Europe and northern Africa: result of a right lateral shear zone between the Appalachians and the Urals. *Geological Society of America Bulletin*, **88**, 1305–1320.
- Balen, D., Massonne, H.-J. & Petrinec, Z., 2015. Collision-related Early Paleozoic evolution of a crustal fragment from the northern Gondwana margin (Slavonian Mts., Tisia Mega-Unit, Croatia): reconstruction of the P-T path, timing and paleotectonic implications. *Lithos*, in press.
- Bertini, G., Elter, F.M. & Talarico, F., 1994. Evidenze di una fase estensionale pre-triassica nel complesso degli gneiss nell'area geotermica di Larderello (Toscana meridionale). *Studi Geologici Camerti, Volume speciale*, **1**, 129-137.
- Borsi, S., Ferrara, G., Rau, A. & Tongiorgi, M., 1967. Determinazioni col metodo Rb/Sr delle filladi e quarziti listate di Buti (Monti Pisani). *Atti della Società toscana di scienze naturali, Memorie, Serie A*, **73**, 632-646.
- Braga, R., Giacomini, F., Messiga, B. & Tribuzio, R., 2001. The Sondalo Gabbroic complex (Central Alps, Northern Italy): evidence for emplacement of mantle-derived melts into amphibolite-facies metapelites. *Physics and Chemistry of the Earth, Part A: Solid Earth and Geodesy* **26**, 333-342.
- Brodie, K. H., Rutter, E. H. & Rex, D., 1989. On the age of deep crustal extensional faulting in the Ivrea zone, northern Italy. *Geological Society, London, Special Publications*, **45**, 203-210.
- Broska, I. & Siman, P., 1998. The breakdown of monazite in the West-Carpathian Veporic orthogneisses and Tatric granites. *Geologica Carpathica*, **49**, 161-167.
- Broska, I., Williams, C.T., Janák, M. & Nagy, G., 2005. Alteration and breakdown of xenotime-(Y) and monazite-(Ce) in granitic rocks of the Western Carpathians, Slovakia. *Lithos*, **82**, 71–83.
- Budzyń, B., Harlov, D. E., Williams, M. L. & Jercinovic, M. J., 2011. Experimental determination of stability relations between monazite, fluorapatite, allanite, and REE-epidote as a function of pressure, temperature, and fluid composition. *American Mineralogist*, **96**, 1547-1567.
- Cadel, G., 1986. Geology and Uranium mineralization of the Collio Basin (Central Southern Alps, Italy). *Uranium*, **2**, 215-540.
- Cadel, G., Cosi, M., Pennacchioni, G. & Spalla, M.I., 1996. A new map of the Permian-Carboniferous cover and Variscan metamorphic basement in the central Orobic Alps, Southern Alps-Italy: structural and stratigraphical data. *Memorie di Scienze Geologiche Padova*, **48**, 1-53.
- Carmignani, L. & Kligfield, R., 1990. Crustal extension in the Northern Apennines: the transition from compression to extension in the Alpi Apuane core complex. *Tectonics*, **9**, 1275-1303.
- Deer, W. A., Howie, R.A. & Zussman, J., 1992. An introduction to the rock-forming minerals (Vol. 696). London, Longman.

- Del Moro, A., Puxeddu, M., Radicati di Brozolo, F. & Villa, I.M., 1982. Rb-Sr and K-Ar ages on minerals at temperatures of 300-400° C from deep wells in the Larderello Geothermal Field (Italy). *Contributions to Mineralogy and Petrology*, **81**, 340-349.
- Deroin, J.P. & Bonin, B., 2003. Late Variscan tectonomagmatic activity in Western Europe and surrounding areas: the Mid-Permian Episode. In Decandia, F.A., Cassinis, G. & Spina A. (Guest eds.), Special Proceedings on «Late Palaeozoic to Early Mesozoic events of Mediterranean Europe, and additional regional reports», April 30th-May 7th 2001, Siena (Italy). *Bollettino Società Geologica Italiana vol. spec.*, **2**, 169-184.
- Doglioni, C., 1984. Tettonica triassica transpressiva nelle Dolomiti. *Giornale di Geologia*, **46**, 47-60.
- Fellin, M.G., Reiners, P.W., Brandon, M.T., Wuthrich, E., Balestrieri, M.L. & Molli, G., 2007. Thermochronologic evidence for exhumational history of the Alpi Apuane metamorphic core complex, northern Apennines, Italy. *Tectonics*, **26**, TC6015.
- Ferrara, G. & Tonarini, S., 1985. Radiometric geochronology in Tuscany: results and problems. *Rendiconti della Società Italiana di Mineralogia e Petrologia*, **40**, 111-124.
- Fiannacca, P., Lo Pò, D., Ortolano, G., Cirrincione, R. & Pezzino, A., 2012. Thermodynamic modeling assisted by multivariate statistical image analysis as a tool for unraveling metamorphic PTd evolution: an example from ilmenite-garnet-bearing metapelite of the Peloritani Mountains, Southern Italy. *Mineralogy and Petrology*, **106**, 151-171.
- Finger, F., Broska, I., Roberts., M.P. & Schermaier, A., 1998. Replacement of primary monazite by apatite-allanite-epidote coronas in an amphibolite facies granite gneiss from the eastern Alps. *American Mineralogist*, **83**, 248-258.
- Franceschini, F., 1998. Evidence of an extensive Pliocene-Quaternary contact metamorphism in Southern Tuscany. *Memorie della Società Geologica Italiana*, **52**, 479-492.
- Gasser, D., Bruand, E., Rubatto, D. & Stüwe, K., 2012. The behaviour of monazite from greenschist facies phyllites to anatectic gneisses: an example from the Chugach Metamorphic Complex, southern Alaska. *Lithos*, **134**, 108-122.
- Gieré, R. & Sorensen, S. S., 2004. Allanite and other REE-rich epidote-group minerals. *Reviews in Mineralogy and Geochemistry*, **56**, 431-493.
- Giorgetti, G., Goffe, B., Memmi, I. & Nieto, F. 1998. Metamorphic evolution of Verrucano metasediments in northern Apennines: new petrological constraints. *European Journal of Mineralogy*, **10**, 1295-1308.
- Godard, G., 2009. Two orogenic cycles recorded in eclogite-facies gneiss from the Southern Armorican Massif (France). *European Journal of Mineralogy*, **21**, 1173-1190.
- Goswami-Banerjee, S. & Robyr, M., 2015. Pressure and temperature conditions for crystallization of metamorphic allanite and monazite in metapelites: a case study from the Miyar Valley (high Himalayan Crystalline of Zaskar, NW India). *Journal of Metamorphic Geology*, **33**, 535-556.
- Handy, M.R. & Zingg, A., 1991. The tectonic and rheological evolution of an attenuated cross section of the continental crust: Ivrea crustal section, southern Alps, north-western Italy and southern Switzerland. *Geological Society of America Bulletin*, **103**, 236-253.
- Hermann, J., Müntener, O. & Günther, D., 2001. Differentiation of mafic magma in a continental crust-to-mantle transition zone. *Journal of Petrology*, **42**, 189-206.
- Janots, E., Brunet, F., Goffé, B., Poinssot, C., Burchard, M. & Cemic, L., 2007. Thermochemistry of monazite-(La) and dissakisite-(La): implications for monazite and allanite stability in metapelites. *Contributions to Mineralogy and Petrology*, **154**, 1-14.

- Janots, E., Engi, M., Berger, A., Allaz, J., Schwarz, J.-O. & Spandler, C., 2008. Prograde metamorphic sequence of REE minerals in pelitic rocks of the Central Alps: implications for allanite–monazite–xenotime phase relations from 250 to 610 °C. *Journal of Metamorphic Geology*, **26**, 509–526.
- Jolivet, L., Faccenna, C., Goffè, B. *et al.*, 1998. Midcrustal shear zones in postorogenic extension: example from the northern Tyrrhenian Sea. *Journal of Geophysical Research*, **103**, 12123–12160.
- Kligfield, R., Hunziker, J., Dallmeyer, R.D. & Schamel, S. 1986. Dating of deformational phases using K-Ar and $^{40}\text{Ar}/^{39}\text{Ar}$ techniques: results from the Northern Apennines. *Journal of Structural Geology*, **8**, 781-798.
- Langone, A., Braga, R., Massonne, H.-J. & Tiepolo, M., 2011. Preservation of old (prograde metamorphic) U-Th-Pb ages in unshielded monazite from the high-pressure paragneisses of the Variscan Ulten Zone (Italy). *Lithos*, **127**, 68-85.
- Liu, Y., Siebel, W., Theye, T. & Massonne, H.-J., 2011. Isotopic and structural constraints on the late Miocene to Pliocene evolution of the Namche Barwa area, eastern Himalayan syntaxis, SE Tibet. *Gondwana Research*, **19**, 894–909.
- Lo Pò, D. & Braga, R., 2014. Influence of ferric iron on phase equilibria in greenschist facies assemblages: the hematite-rich metasedimentary rocks from the Monti Pisani (Northern Apennines). *Journal of Metamorphic Geology*, **32**, 371-387.
- Lo Pò, D., Braga, R. & Massonne H.-J., 2015. Petrographic, mineral and pressure–temperature constraints on phyllites from the Variscan basement at Punta Bianca, Northern Apennines, Italy. *Italian Journal of Geosciences*. DOI: 10.3301/IJG.2015.29
- Ludwig, K.R., 2012. User's Manual for Isoplot 3.75. A Geochronological Toolkit for Microsoft Excel. Berkeley Geochronology Center. Special Publication No. 5.
- Majka, J. & Budzyn, B., 2006. Monazite Breakdown in Metapelites From Wedel Jarlsberg Land, Svalbard-Preliminary Report. *Mineralogia*, **37**, 61.
- Marroni, M., Molli, G., Montanini, A. & Tribuzio, R., 1998. The association of continental crust rocks with ophiolites (Northern Apennines, Italy): Implications for the continent-ocean transition. *Tectonophysics*, **29**, 43-66.
- Massari, F., 1986. Some thoughts on the Permo-Triassic evolution of the South Alpine area (Italy). *Memorie della Società Geologica Italiana*, **34**, 179–188
- Massonne, H.-J., 2013. Constructing the pressure–temperature path of ultrahigh-pressure rocks. *Elements*, **9**, 267-272.
- Massonne, H.-J., 2014. Wealth of P-T-t information in medium-high grade metapelites: example from the Jubrique Unit of the Betic Cordillera, S Spain. *Lithos*, **208-209**, 137-152.
- Massonne, H.-J., Kennedy, A., Nasdala, L., Theye, T. & 2007. Dating of zircon and monazite from diamondiferous quartzofeldspathic rocks of the Saxonian Erzgebirge. *Mineralogical Magazine*, **71**, 407–425.
- Matte, P., 2001. The Variscan collage and orogeny (480-290 Ma) and the tectonic definition of the Armorica microplate: a review. *Terra Nova*, **13**, 112-128.
- McCann, T., Pascal, C., Timmerman, M.J. *et al.*, 2006. Post-Variscan (end Carboniferous – Early Permian) basin evolution in Western and Central Europe. In Gee, D.G. & Stephenson, R.A. (eds), European Lithosphere Dynamics. *Geological Society of London, Memoirs*, **32**, 355-388.

- Mohn, G., Manatschal, G., Beltrando, M., Masini, E. & Kuszniir, N., 2012. Necking of continental crust in magma-poor rifted margins: Evidence from the fossil Alpine Tethys margins. *Tectonics*, **31**, TC1012.
- Molli, G., 2002. Field Trip Eastern Liguria/Alpi Apuane. Gordon Research Conference on Rock Deformation. Il Ciocco, Barga, Italy, CNR Report, 58 pp.
- Molli, G., 2008. Northern Apennine-Corsica orogenic system: an updated overview. In Siegesmund, S., Fugenschuh, B., Froitzheim, N. (eds) Tectonic Aspects of the Alpine-Dinaride-Carpathian System. *Geological Society, Special Publications*, **298**, 413-442.
- Molli, G., Giorgetti, G. & Meccheri, M., 2000. Structural and petrological constraints on the tectono-metamorphic evolution of the Massa Unit (Alpi Apuane, NW Tuscany, Italy). *Geological Journal*, **35**, 251-264.
- Molli, G., Montanini, A. & Frank W., 2002. MORB-derived Variscan amphibolites in the Northern Apennine Basement: the Cerreto metamorphic slices (Tuscan-Emilian Apennine, NW Italy). *Ophioliti*, **27**, 17-30.
- Monjoie, P., Bussy, F., Lapierre, H. & Pfeifer, H.R., 2005. Modeling of in situ crystallization processes in the Permian mafic layered intrusion of Mont Collon (Dent Blanche nappe, western Alps). *Lithos*, **83**, 317-346.
- Montanini, A. & Tribuzio, R., 2001. Gabbro-derived and felsic granulites from the Northern Apennines (Italy): evidence for emplacement of tholeiitic basalts in the post-Variscan lower crust. *Journal of Petrology*, **42**, 2259-2277.
- Montel, J.-M., Foret, S., Veschambre, M., Nicollet, C. & Provost, A., 1996. Electron microprobe dating of monazite. *Chemical Geology*, **131**, 37-53.
- Musumeci, G., Mazzarini, F., Tiepolo, M. & Di Vincenzo, G., 2011. U-Pb and ^{40}Ar - ^{39}Ar geochronology of Palaeozoic units in the northern Apennines: determining protolith age and alpine evolution using the Calamita Schist and Ortano Porphyroid. *Geological Journal*, **46**, 288-310.
- Ondrejka, M., Uher, P., Putiš, M., Broska, I., Bačík, P., Konečný, P. & Schmiedt, I., 2012. Two-stage breakdown of monazite by post-magmatic and metamorphic fluids: An example from the Veporic orthogneiss, Western Carpathians, Slovakia. *Lithos*, **142**, 245-255.
- Pandeli, E., Gianelli, G. & Morelli, M., 2005. The crystalline units of the middle-upper crust of the Larderello geothermal region (southern Tuscany, Italy): new data for their classification and tectono-metamorphic evolution. *Bollettino Della Società Geologica Italiana*, **3**, 139-155.
- Peressini, G., Quick, J. E., Sinigoi, S., Hofmann, A. W. & Fanning, M., 2007. Duration of a large mafic intrusion and heat transfer in the lower crust: a SHRIMP U-Pb zircon study in the Ivrea-Verbano Zone (Western Alps, Italy). *Journal of Petrology*, **48**, 1185-1218.
- Piccardo, G.B., Padovano, M. & Guarnieri, L., 2014. The Ligurian Tethys: Mantle processes and geodynamics. *Earth-Science Reviews*, **138**, 409-434.
- Pyle, J.M. & Spear, F.S., 2000. An empirical garnet (YAG) \pm xenotime thermometer. *Contributions to Mineralogy and Petrology*, **138**, 51-58.
- Rasmussen, B. & Muhling, J.R., 2007. Monazite begets monazite: evidence for the dissolution of detrital monazite and reprecipitation of syntectonic monazite during low-grade regional metamorphism. *Contributions to Mineralogy and Petrology*, **154**, 675-689.
- Rau, A., 1990. Evolution of the Tuscan domain between the Upper Carboniferous and the Middle Triassic: a new hypothesis. *Bollettino Società Geologica Italiana*, **109**, 231-238.

- Renna, M.R., Tribuzio, R. & Braga, R., 2013. Petrogenetic relationships between peralkaline rhyolite dykes and mafic rocks in the post-Variscan gabbroic complex from Bocca di Tenda (northern Corsica, France). *Contributions to Mineralogy and Petrology*, **165**, 1073 – 1085.
- Schmid, S., 1993. Ivrea Zone and adjacent southern Alpine basement. In von Raumer, J.F. Neubauer, F. (eds), *Pre-Mesozoic Geology in the Alps*, Springer, Berlin, 567-584.
- Shaw, D.M., 1956. Geochemistry of pelitic rocks. Part III. Major elements and general geochemistry. *Geological Society of America Bulletin*, **67**, 919–934.
- Spear, F.S. & Pyle, J.M., 2010. Theoretical modeling of monazite growth in a low-Ca metapelite. *Chemical Geology*, **273**, 111-119.
- Stüwe, K., 1997. Effective bulk composition change due to cooling: a model predicting complexities in retrograde reaction textures. *Contributions to Mineralogy and Petrology*, **129**, 43–52.
- Theye, T., Reinhardt, J., Goffe, B., Jolivet, L. & Brunet, C., 1997. Ferro- and magnesiocarpholite from the Monte Argentario (Italy): first evidence for high-pressure metamorphism of the metasedimentary Verrucano sequence, and significance for P-T path reconstruction. *European Journal of Mineralogy*, **9**, 859–873.
- Tribuzio, R., Renna, M.R., Braga, R. & Dallai, L., 2009. Petrogenesis of Early Permian olivine-bearing cumulates and associated basalt dykes from Bocca di Tenda (Northern Corsica): implications for post-collisional Variscan evolution. *Chemical Geology*, **259**, 190-203.
- Upadhyay, D., & Pruseth, K.L., 2012. Fluid-induced dissolution breakdown of monazite from Tso Moriri complex, NW Himalayas: evidence for immobility of trace elements. *Contributions to Mineralogy and Petrology*, **164**, 303-316.
- Vance, D., Müller, W. & Villa, I.M., 2003. Geochronology: linking the isotopic record with petrology and textures - an introduction. In Vance, D., Midler, W. & Villa, I. M. (eds) 2003. *Geochronology: Linking the Isotopic Record with Petrology and Textures*. Geological Society, London, *Special Publications*, **220**, 1-24.
- Williams, M.L., Jercinovic, M.J., Goncalves, P. & Mahan, K. 2006. Format and philosophy for collecting, compiling, and reporting microprobe monazite ages. *Chemical Geology*, **22**, 1-15.
- Williams, M.L., Jercinovic, M.J. & Hetherington, C.J., 2007. Microprobe monazite geochronology: understanding geologic processes by integrating composition and chronology. *Annual Review of Earth and Planetary Sciences*, **35**, 137-175.
- Williams, M.L., Jercinovic, M.J., Harlov, D.E., Budzyń, B. & Hetherington, C.J., 2011. Resetting monazite ages during fluid-related alteration. *Chemical Geology*, **283**, 218-225.
- Wing, B.A., Ferry, J.M. & Harrison, T.M., 2003. Prograde destruction and formation of monazite and allanite during contact and regional metamorphism of pelites: petrology and geochronology. *Contributions to Mineralogy and Petrology*, **145**, 228-250.
- Ziegler, P.A., 1986. Geodynamic model for the Paleozoic crustal consolidation of Western and Central Europe. *Tectonophysics*, **126**, 303-328.

SUPPORTING INFORMATION

Additional supporting information can be found in the online version of this article at the publisher's

web site:

Appendix S1. Analytical procedures.

Appendix S2. Calculation of the bulk rock chemistry.

Appendix S3. Input parameters for phase diagram calculations.

Figure S1. BSE images of K-feldspar exsolutions within a plagioclase grain.

Figure S2. Whole-rock Ca and Al compositions referred to the average pelite of Shaw (1956) of metapelites from the biotite- and garnet-zone studied by Wing *et al.* (1993). The Pontremoli7 sample lies on the line in which monazite and allanite coexist, in agreement with the observed mineralogy.

Received 24 July 2015; revision accepted 3 November 2015.

FIGURE AND TABLE CAPTIONS

Figure 1

Geological framework of the Northern Apennine. The Variscan basement is in black.

Figure 2

Petrography of the Pontremoli garnet micaschist. (a) Muscovite and chlorite surrounding a garnet porphyroblast (sample AG7, BSE image); (b) decussate aggregate of muscovite (sample Pontremoli7, crossed polars photomicrograph); (c) relationships between S_1 and S_2 (sample Pontremoli 8, BSE image); (d) corona around monazite in the matrix (sample Pontremoli7, BSE image); (e) xenotime inclusions within the garnet inner core (sample Pontremoli7, BSE image); (f) epidote around allanite in the retrogressed garnet rim (sample Pontremoli7, BSE image).

Figure 3

Chemical diagrams of garnet and muscovite in Pontremoli7. (a) Compositional profile showing contents of almandine, spessartine, pyrope, and grossular components along a garnet transect; (b) Y and P profile along the same transect; (c) Si vs. Mg plot for muscovite in different microstructural positions; (d) Si vs. Na for the same muscovite crystals.

Figure 4

X-ray maps of garnet and muscovite in Pontremoli7. (a) Mn in garnet; (b) Ca in garnet; (c) Y in garnet; (d) Mg in muscovite along the main schistosity; (e) Na in muscovite along the main schistosity. The location of muscovite analyses along the main schistosity reported in Table 2 is shown.

Figure 5

BSE images and schematic representations of the coronitic microstructure involving monazite (sample Pontremoli7).

Figure 6

BSE images and Ce-Th-Y X-ray maps of three monazite grains in Pontremoli7: (a) Mnz01; (b) Mnz02; (c) Mnz04.

Figure 7

BSE images reporting the microstructural occurrences and the locations of analyses in monazite in Pontremoli7: (a) Mnz01; (b) Mnz02; (c) Mnz04; (d) Mnz03. The labels in brackets refer to the name of the point analyses, while the numbers below refer to the corresponding date. Note that Mnz01, Mnz02, Mnz04 are located in the matrix, whereas Mnz03 is within the retrogressed garnet rim and there is no age because of the low U and Pb.

Figure 8

Monazite composition and EMP dates. (a) UO_2 vs. ThO_2 diagram of the monazite in Pontremoli7 sample compared to other monazite occurrences (Rasmussen & Muhling, 2007; Janots *et al.*, 2008; Langone *et al.*, 2011); (b) Y_2O_3 vs. ThO_2 diagram of monazite (labels refer to the obtained dates); (c) dates vs. ThO_2 diagram of monazite in the retrogressed garnet rim; (d) relative probability plot and histogram of the monazite EMP dates obtained using the Isoplot/Ex program, v. 3.75 (Ludwig, 2012).

Figure 9

P - T pseudosection calculated with the unfractionated bulk-composition (bulk1). The intersection is related to the P - T range obtained by using the inner core garnet isopleths. A P - T uncertainty ellipse is also displayed. Mineral abbreviations are Ms (K-white mica), Chl (chlorite), Pg (Na-white mica), Grt (garnet), Bt (biotite), Pl (plagioclase), Kf (K-feldspar), Ilm (ilmenite), Rt (rutile), Ttn (titanite), Lws (lawsonite), Zo (zoisite), And (andalusite), Sil (sillimanite), St (staurolite), Cld (chloritoid), Crd (cordierite).

Figure 10

P - T pseudosection calculated for the effective composition bulk2. The ellipse corresponds to the P - T uncertainty related to the garnet rim isopleth intersection. An isopleth for the maximum Si content in the muscovite core (Na-rich) is also displayed. Mineral abbreviations are as in Fig. 9.

Figure 11

P - T pseudosection calculated for the effective composition bulk3. Maximum Si content in the muscovite rim (Mg-rich) and the minimum XFe in chlorite allow the estimation of the pressure peak. The ellipse represents the P - T uncertainty. Retrograde paragenesis is delimited by the green line. Mineral abbreviations are as in Fig. 9.

Figure 12

Scheme showing the main petrographic and chemical constraints and the derived P - T conditions.

Figure 13

Two possible P - T - t paths for the obtained P - T constraints: (a) monometamorphic anticlockwise P - T evolution; (b, c) two polymetamorphic clockwise P - T - t trajectories separated by an intermediate retrograde stage. Late paragenesis is the observed retrograde assemblage (muscovite + chlorite + albite + ilmenite + quartz). MnzI and Mnz II are respectively the U-Th-bearing monazite and U-Th-poor monazite. The dashed lines refer to inferred trajectories.

Table 1

Mineral compositions of garnet in Pontremoli7 normalized to 8 cations. Fe^{3+} is equal to $4 - \text{Al}$. b.d.l. = below the detection limit; n.c. = not calculated.

Table 2

Structural formulae of potassic white mica in Pontremoli7 calculated on the basis of 22 oxygens. Fe^{3+} is stoichiometric-estimated considering $\text{Fe}^{3+} = 42 - \text{sum of the valences (Si, Ti, Cr, Al, Mn, Mg, Fe)-Ba-Ca}$.

Table 3

Structural formulae of chlorite in Pontremoli7 calculated on the basis of 28 oxygens and the negligence of Na and Ca. Chlorite is assumed to be completely hydrated (16 H).

Table 4

Structural formulae of plagioclase in Pontremoli7 based on 8 oxygens.

Table 5

EMP mineral chemistry and dates of monazite in Pontremoli7 on the basis of 4 oxygen.

Table 6

Calculated bulk-rock compositions with garnet (bulk 1) and without garnet core (bulk2) and the whole garnet (bulk3).

Footnote: To convert vol. % in wt. % the densities of minerals reported in Anthony *et al.* (2011) were used. The densities of the minerals that show significant solid solution were calculated through a linear interpolation between the densities of the corresponding end-members.

Table 1

Garnet	rim			outer core			inner core		
	gt1_01a	gt1_01b	gt1_01c	gt1_04	gt1_05	gt1_05b	gt1_09b	gt1_10a	gt1_11b
Point analyses									
wt. %									
SiO ₂	35.69	35.82	35.35	35.46	35.44	35.30	35.13	34.77	34.95
Al ₂ O ₃	21.02	21.35	20.96	21.16	21.03	21.02	20.65	20.78	20.77
Fe ₂ O ₃	3.04	3.00	3.86	3.81	3.61	3.88	2.73	2.98	2.71
TiO ₂	0.06	0.05	0.06	0.08	0.08	0.07	0.07	0.06	0.07
FeO	36.00	36.02	35.24	33.37	33.18	31.69	29.90	29.41	29.55
MnO	0.10	0.15	0.39	1.31	1.59	2.44	4.86	4.96	5.16
MgO	2.51	2.13	1.88	1.44	1.36	1.24	1.08	1.06	1.04
CaO	1.73	2.30	2.63	4.10	4.10	4.64	4.15	4.15	4.08
P ₂ O ₅	0.03	0.02	0.02	0.02	b.d.l.	0.02	b.d.l.	b.d.l.	b.d.l.
Y ₂ O ₃	b.d.l.	b.d.l.	b.d.l.	b.d.l.	b.d.l.	b.d.l.	0.77	0.80	0.85
Dy ₂ O ₃	b.d.l.	b.d.l.	b.d.l.	b.d.l.	b.d.l.	b.d.l.	b.d.l.	b.d.l.	0.11
Er ₂ O ₃	b.d.l.	b.d.l.	0.00	b.d.l.	b.d.l.	b.d.l.	0.13	0.14	0.12
Yb ₂ O ₃	b.d.l.	0.01	0.01	b.d.l.	b.d.l.	b.d.l.	0.13	0.11	0.15
Total	100.20	100.89	100.41	100.78	100.44	100.29	99.67	99.29	99.58
ppm									
P	150	90	70	90	n.c.	70	n.c.	n.c.	n.c.
Ti	350	320	350	470	490	400	390	370	430
Y	n.c.	n.c.	n.c.	n.c.	n.c.	n.c.	6040	6320	6720
Dy	n.c.	n.c.	n.c.	n.c.	n.c.	n.c.	n.c.	n.c.	980
Er	n.c.	n.c.	n.c.	n.c.	n.c.	n.c.	1130	1190	1090
Yb	n.c.	n.c.	n.c.	n.c.	n.c.	n.c.	1112	962	1293
apfu									
Si	2.90	2.89	2.87	2.87	2.88	2.87	2.89	2.87	2.88
P	0.00	0.00	0.00	0.00	0.00	0.00	0.00	0.00	0.00
Al ^{IV}	0.11	0.11	1.88	0.13	0.12	0.13	0.11	0.13	0.12
Al ^{VI}	1.91	1.92	0.24	1.89	1.89	1.88	1.89	1.89	1.90
Fe ³⁺	0.19	0.18	0.00	0.23	0.22	0.24	0.17	0.19	0.17
Fe ²⁺	2.44	2.43	2.40	2.26	2.25	2.15	2.06	2.03	2.04
Mn	0.01	0.01	0.03	0.09	0.11	0.17	0.34	0.35	0.36
Mg	0.30	0.26	0.23	0.17	0.16	0.15	0.13	0.13	0.13
Ca	0.15	0.20	0.23	0.36	0.36	0.40	0.37	0.37	0.36
Alm	0.84	0.84	0.84	0.78	0.78	0.75	0.70	0.70	0.69
Adr	0.09	0.09	0.10	0.11	0.10	0.11	0.08	0.09	0.08
Grs	0.00	0.00	0.00	0.01	0.02	0.03	0.04	0.04	0.04
Sps	0.00	0.00	0.01	0.03	0.04	0.06	0.12	0.12	0.12
Pyr	0.10	0.09	0.09	0.06	0.06	0.05	0.05	0.04	0.04

Table 2

K-white mica								
Point analyses	Schistosity				Decussate structure			
	Type I		Type II		Type I		Type II	
	Ms37_01	Ms37_22	Ms38_01	Ms38_02	Ms45_05	Ms45_06	Ms44_01	Ms44_02
SiO ₂	45.95	46.06	46.79	47.07	45.76	45.58	46.76	46.59
TiO ₂	0.48	0.48	0.35	0.33	0.38	0.40	0.36	0.31
Al ₂ O ₃	35.50	35.28	32.25	32.42	36.23	36.28	32.93	32.83
FeO	1.24	1.03	2.20	2.13	0.86	0.82	1.71	1.58
Fe ₂ O ₃	0.00	0.00	0.00	0.00	0.00	0.00	0.00	0.00
MnO	0.00	0.00	0.00	0.00	0.00	0.01	0.02	0.00
MgO	0.90	0.89	1.61	1.54	0.61	0.63	1.29	1.36
CaO	0.00	0.02	0.01	0.00	0.02	0.03	0.00	0.01
Na ₂ O	2.23	2.14	0.86	0.91	2.22	2.24	0.87	0.72
K ₂ O	8.33	8.63	10.13	9.88	8.38	8.19	10.08	10.45
BaO	0.19	0.18	0.20	0.16	0.22	0.25	0.17	0.18
Total	94.81	94.81	94.81	94.81	94.68	94.42	94.19	94.04
Si	6.12	6.15	6.32	6.34	6.09	6.08	6.31	6.31
Al ^{IV}	1.88	1.86	1.68	1.66	1.91	1.92	1.69	1.69
Al ^{VI}	3.69	3.69	3.46	3.48	3.77	3.78	3.55	3.55
Ti	0.05	0.05	0.04	0.03	0.04	0.04	0.04	0.03
Fe ²⁺	0.14	0.12	0.25	0.24	0.10	0.09	0.19	0.18
Fe ³⁺	0.00	0.00	0.00	0.00	0.00	0.00	0.00	0.00
Mn	0.00	0.00	0.00	0.00	0.00	0.00	0.00	0.00
Mg	0.18	0.18	0.32	0.31	0.12	0.13	0.26	0.28
Ca	0.00	0.00	0.00	0.00	0.03	0.01	0.00	0.00
Ba	0.01	0.01	0.01	0.01	0.01	0.01	0.01	0.01
Na	0.58	0.55	0.26	0.24	0.57	0.58	0.23	0.19
K	1.41	1.47	1.75	1.70	1.42	1.39	1.74	1.81

K-white mica		
Point analyses	Garnet rim	
	Type II	
	Ms46_01	Ms46_02
SiO ₂	46.57	46.81
TiO ₂	0.24	0.29
Al ₂ O ₃	35.22	33.94
FeO	1.55	1.87
Fe ₂ O ₃	0.00	0.00
MnO	0.03	0.00
MgO	0.85	1.19
CaO	0.02	0.00
Na ₂ O	0.76	0.81
K ₂ O	10.07	9.92
BaO	0.24	0.18
Total	95.55	95.00
Si	6.18	6.25
Al ^{IV}	1.82	1.75
Al ^{VI}	3.68	3.58
Ti	0.02	0.03
Fe ²⁺	0.17	0.21
Fe ³⁺	0.00	0.00
Mn	0.00	0.00
Mg	0.17	0.24
Ca	0.00	0.00
Ba	0.01	0.01
Na	0.20	0.21
K	1.70	1.69

Table 3

Chlorite						
Point analyses	Schistosity		Decussate structure		Garnet rim	
	Chl01	Chl02	Chl10	Chl03	Chl07	Chl08
SiO ₂	23.53	24.22	24.01	24.12	24.05	23.74
TiO ₂	0.06	0.08	0.07	0.07	0.07	0.04
Al ₂ O ₃	20.67	21.72	20.95	20.84	21.03	21.86
FeO	31.76	31.26	31.63	30.08	29.51	31.58
MnO	0.18	0.13	0.14	0.10	0.10	0.09
MgO	10.65	11.30	11.26	11.53	12.41	10.57
Total	86.84	88.71	88.07	86.73	87.17	87.89
Si	5.22	5.22	5.23	5.30	5.24	5.18
Al ^{IV}	2.78	2.79	2.77	2.71	2.77	2.83
Al ^{VI}	2.62	2.73	2.61	2.68	2.63	2.79
Ti	0.01	0.01	0.01	0.01	0.01	0.01
Fe	5.89	5.63	5.76	5.52	5.37	5.76
Mn	0.03	0.02	0.03	0.02	0.02	0.02
Mg	3.52	3.63	3.66	3.77	4.03	3.44

Table 4

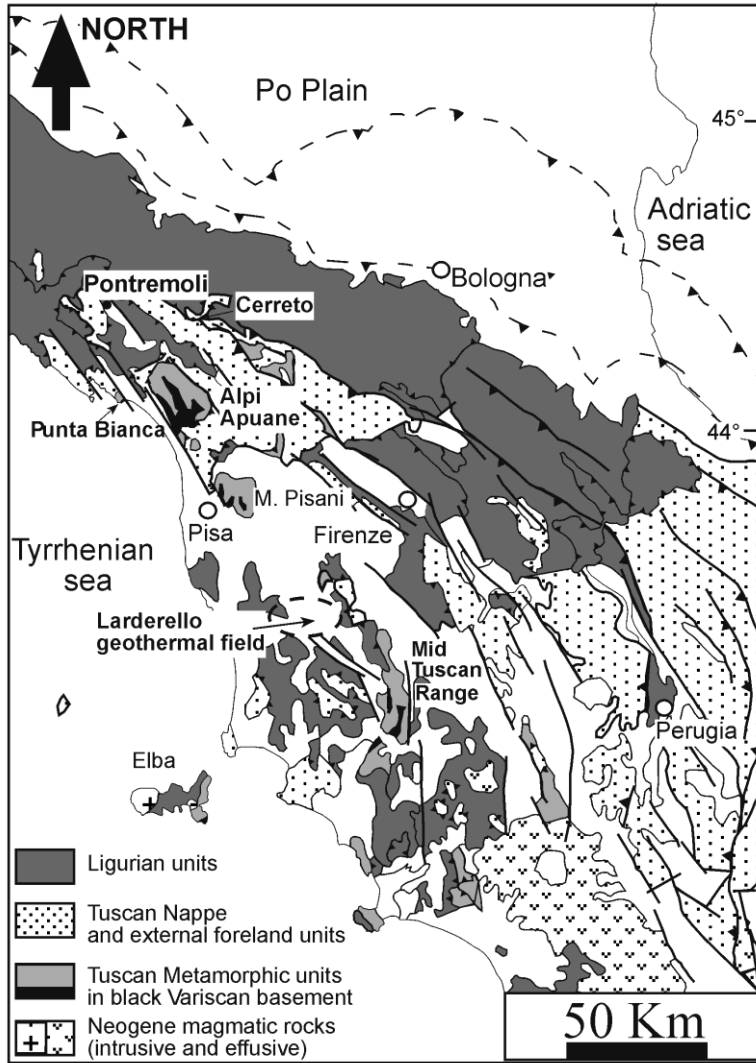
Plagioclase	Core			Rim			Matrix	
	PI02_03	PI02_04	PI01_04	PI01	PI04	PI05	PI07	PI08
SiO ₂	66.27	66.60	66.30	68.59	68.74	68.86	68.74	68.76
Al ₂ O ₃	21.40	21.52	21.32	19.31	19.28	19.30	19.05	19.29
Fe ₂ O ₃	0.05	0.09	0.10	0.13	b.d.l.	0.04	0.13	0.15
CaO	1.98	2.01	2.20	0.33	0.20	0.15	0.12	0.25
Na ₂ O	10.94	10.91	10.88	11.81	11.86	12.01	12.34	12.08
K ₂ O	0.07	0.05	0.05	0.02	0.02	0.00	0.05	0.03
BaO	b.d.l.	0.02	b.d.l.	b.d.l.	b.d.l.	b.d.l.	b.d.l.	b.d.l.
Total	100.71	101.20	100.86	100.18	100.11	100.36	100.44	100.55
Si	2.89	2.89	2.89	2.99	3.00	3.00	3.00	2.99
Al	1.10	1.10	1.10	0.99	0.99	0.99	0.98	0.99
Fe ³⁺	0.00	0.00	0.00	0.00	n.c.	0.00	0.00	0.01
Ba	n.c.	0.00	n.c.	n.c.	n.c.	n.c.	n.c.	n.c.
Ca	0.09	0.09	0.10	0.02	0.01	0.01	0.01	0.01
Na	0.93	0.92	0.92	1.00	1.00	1.01	1.04	1.02
K	0.00	0.00	0.00	0.00	0.00	0.00	0.00	0.00

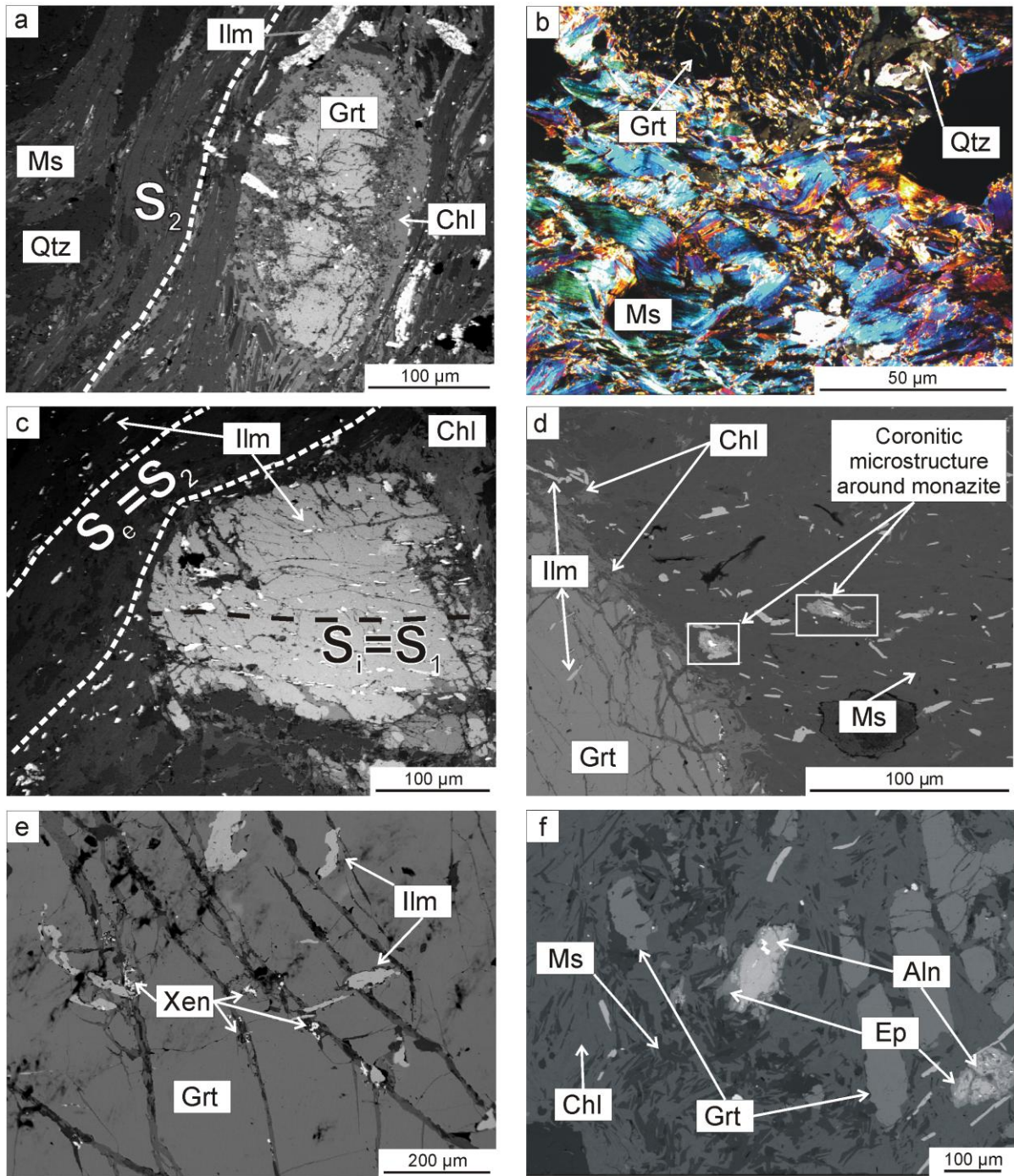
Table 5

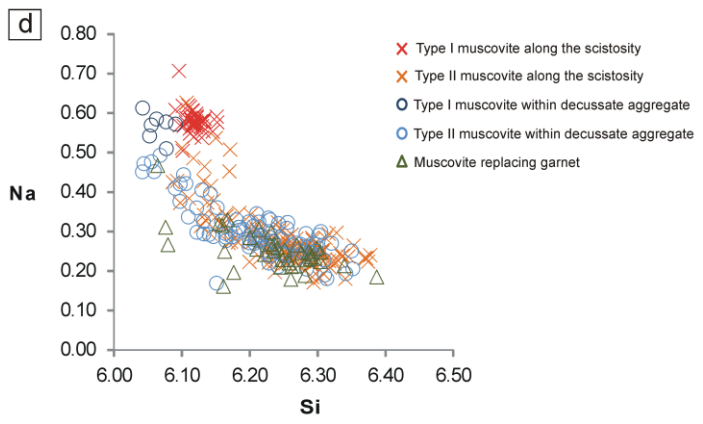
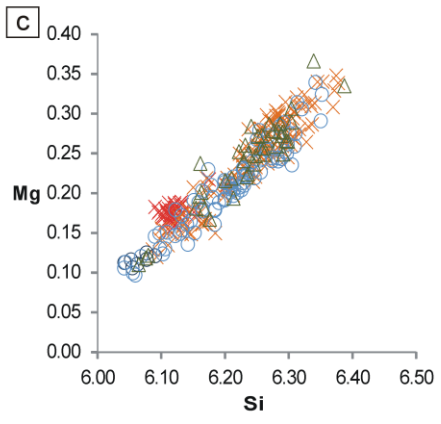
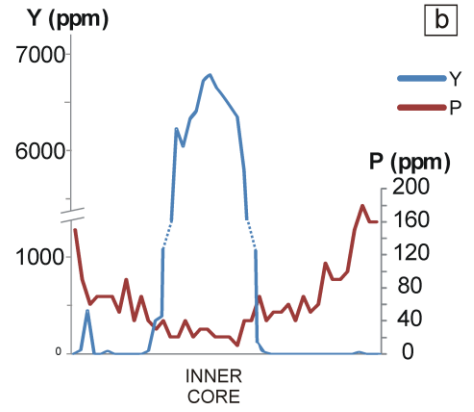
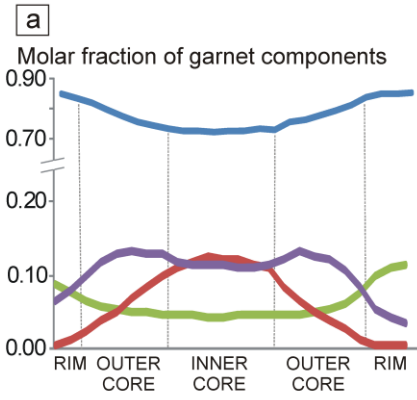
Analysis	Mnz01_01	Mnz04_01	Mnz02_05	Mnz01_01a	Mnz01_02a	Mnz01_05a	Mnz02_01a	Mnz02_04a	Mnz02_09a	Mnz04_04a	Mnz03_02a	Mnz03_03a
SiO ₂	0.66	0.58	0.72	0.78	0.81	0.79	0.81	0.58	0.71	0.49	0.94	0.99
P ₂ O ₅	29.07	29.34	29.40	27.44	27.30	26.75	30.00	29.98	29.96	30.51	28.99	27.10
SO ₃	0.04	0.03	0.02	0.03	0.02	0.03	0.03	0.03	0.02	0.02	0.04	0.03
CaO	1.53	1.54	1.33	1.52	1.58	1.80	1.36	1.47	1.42	1.40	0.52	3.16
Y ₂ O ₃	0.07	0.05	0.03	0.09	0.09	0.05	0.06	0.01	0.04	0.09	0.31	0.32
La ₂ O ₃	13.72	14.56	15.31	14.01	13.42	13.37	14.81	15.39	15.14	14.69	16.91	16.40
Ce ₂ O ₃	27.73	28.64	29.41	27.83	27.53	26.66	28.06	29.16	29.34	29.02	32.51	31.68
Pr ₂ O ₃	3.01	3.05	3.06	2.93	2.65	2.94	3.10	3.04	3.08	3.09	3.33	3.00
Nd ₂ O ₃	11.98	11.95	11.59	11.82	11.48	11.55	12.00	11.63	11.50	12.19	12.59	12.49
Sm ₂ O ₃	2.17	2.11	1.60	2.01	2.05	2.11	2.07	1.54	1.50	2.15	1.89	1.86
Gd ₂ O ₃	1.66	1.54	0.84	1.53	1.57	1.50	1.50	0.79	0.86	1.59	1.11	1.12
Dy ₂ O ₃	0.23	0.20	0.12	0.25	0.27	0.21	0.20	0.11	0.10	0.27	0.31	0.36
PbO	0.13	0.10	0.09	0.12	0.13	0.13	0.10	0.11	0.09	0.09	b.d.l.	0.02
ThO ₂	8.20	6.89	7.32	8.26	9.08	9.62	6.66	7.44	7.69	5.87	1.33	2.22
UO ₂	0.45	0.42	0.38	0.49	0.48	0.50	0.30	0.42	0.39	0.43	b.d.l.	b.d.l.
Tot	100.65	100.99	101.22	99.11	98.46	98.02	101.05	101.70	101.84	101.88	100.79	100.75
Si	0.03	0.02	0.03	0.03	0.03	0.03	0.03	0.02	0.03	0.02	0.04	0.04
P	0.97	0.97	0.97	0.95	0.95	0.94	0.98	0.98	0.98	0.99	0.96	0.91
S	0.00	0.00	0.00	0.00	0.00	0.00	0.00	0.00	0.00	0.00	0.00	0.00
Ca	0.06	0.07	0.06	0.07	0.07	0.08	0.06	0.06	0.06	0.06	0.02	0.14
Y	0.00	0.00	0.00	0.00	0.00	0.00	0.00	0.00	0.00	0.00	0.01	0.01
La	0.20	0.21	0.22	0.21	0.20	0.20	0.21	0.22	0.22	0.21	0.24	0.24
Ce	0.40	0.41	0.42	0.42	0.41	0.40	0.40	0.41	0.41	0.41	0.47	0.46
Pr	0.04	0.04	0.04	0.04	0.04	0.04	0.04	0.04	0.04	0.04	0.05	0.04
Nd	0.17	0.17	0.16	0.17	0.17	0.17	0.17	0.16	0.16	0.17	0.18	0.18
Sm	0.03	0.03	0.02	0.03	0.03	0.03	0.03	0.02	0.02	0.03	0.03	0.03
Gd	0.02	0.02	0.01	0.02	0.02	0.02	0.02	0.01	0.01	0.02	0.01	0.02
Dy	0.00	0.00	0.00	0.00	0.00	0.00	0.00	0.00	0.00	0.00	0.00	0.01
Pb	0.00	0.00	0.00	0.00	0.00	0.00	0.00	0.00	0.00	0.00	n.c.	n.c.
Th	0.07	0.06	0.07	0.08	0.09	0.09	0.06	0.07	0.07	0.05	0.01	0.02
U	0.00	0.00	0.00	0.00	0.00	0.01	0.00	0.00	0.00	0.00	n.c.	n.c.
Dates	311.5	289.6	19.2	292.1	294.4	281.3	294.8	293.1	250.4	307.4	n.c.	n.c.
statistical error	6.5	7.2	0.3	6.2	5.9	5.7	7.7	6.8	6.5	8.0	n.c.	n.c.

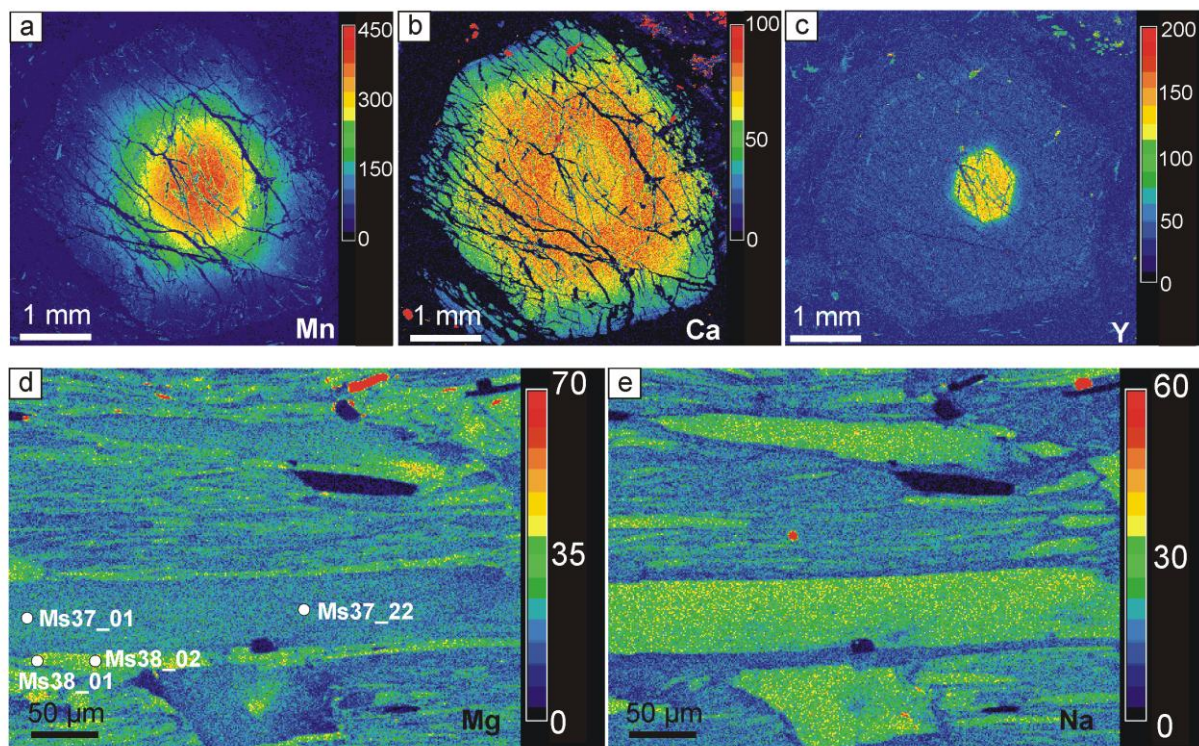
Table 6

	unfractionated composition (bulk1)	fractionated compositions	
		garnet inner and outer core fract. (bulk2)	whole garnet fract. (bulk3)
	wt. %	wt. %	wt. %
SiO ₂	53.31	57.03	57.85
TiO ₂	1.17	1.31	1.36
Al ₂ O ₃	24.22	24.18	24.32
FeO	12.00	8.26	7.13
MnO	0.44	0.03	0.00
MgO	2.56	2.71	2.72
CaO	0.62	0.09	0.00
Na ₂ O	1.19	1.33	1.38
K ₂ O	4.49	5.06	5.25

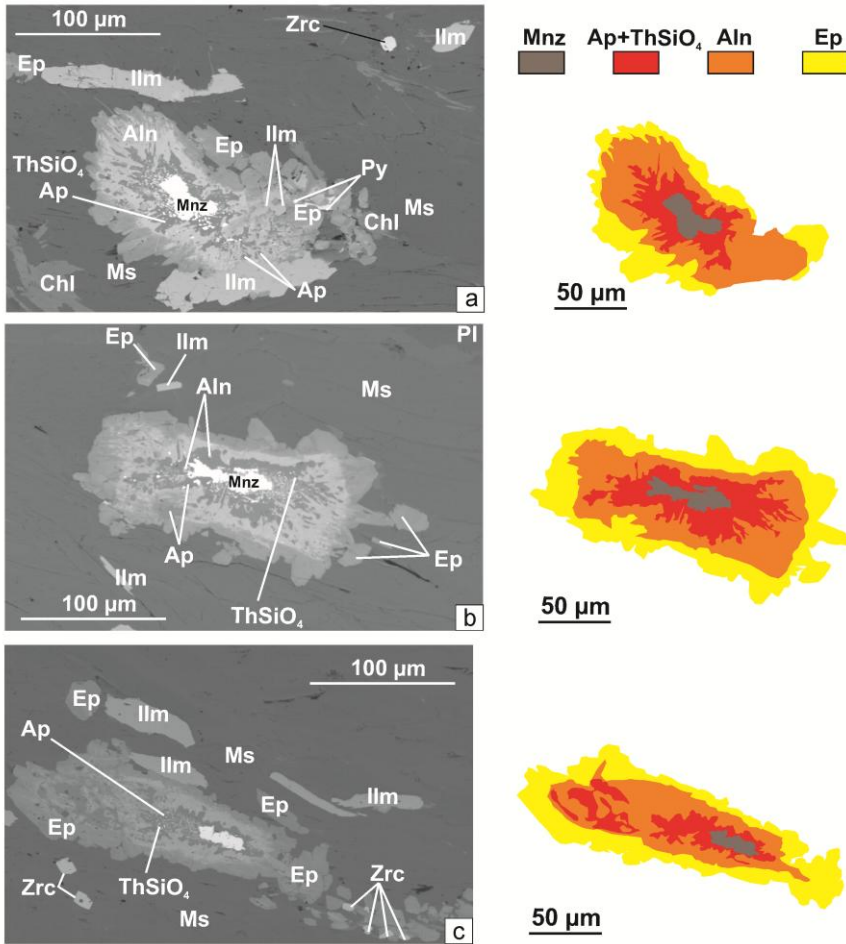




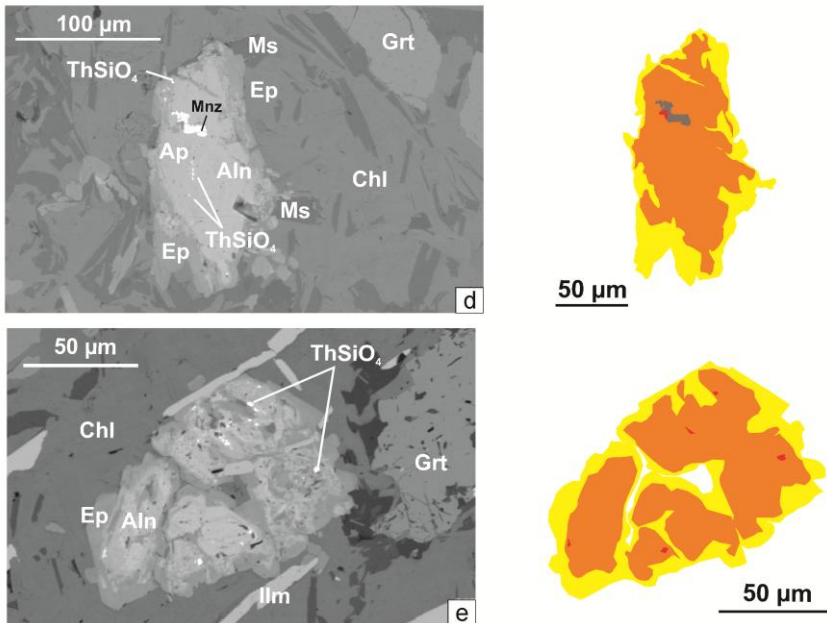


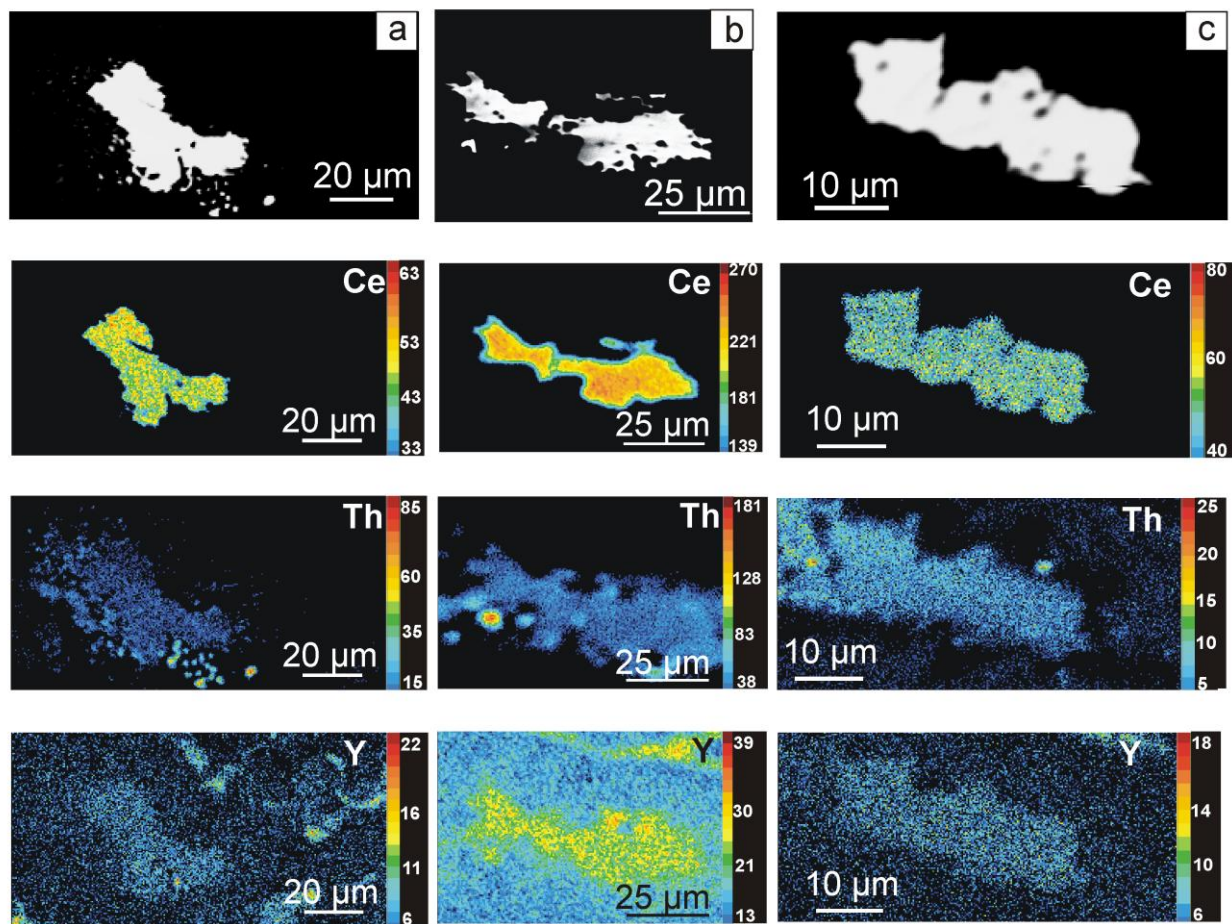


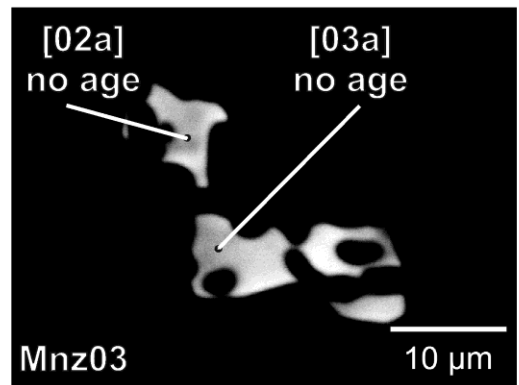
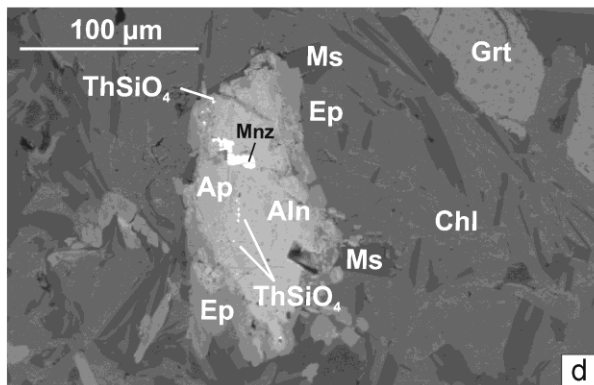
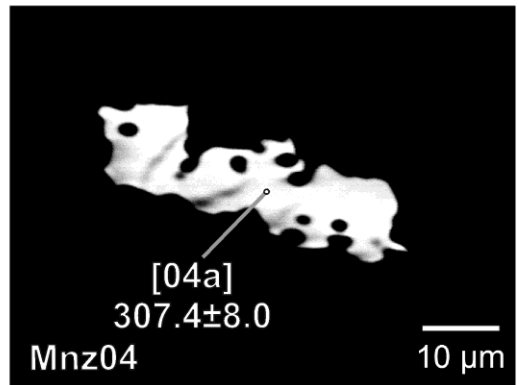
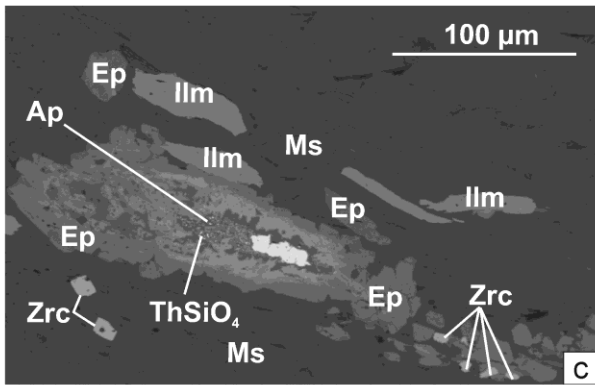
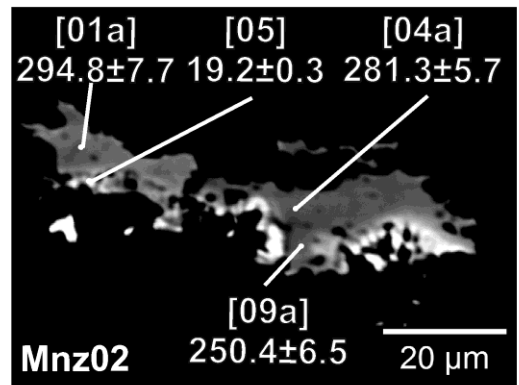
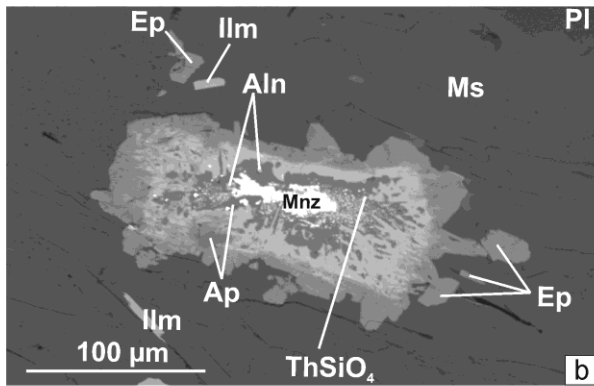
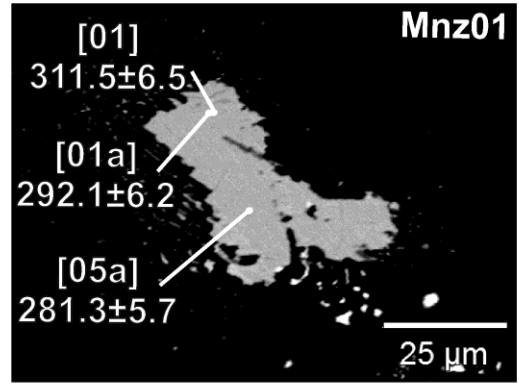
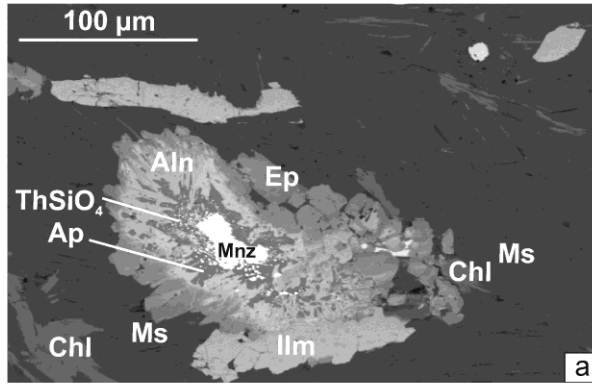
Microstructural site: matrix

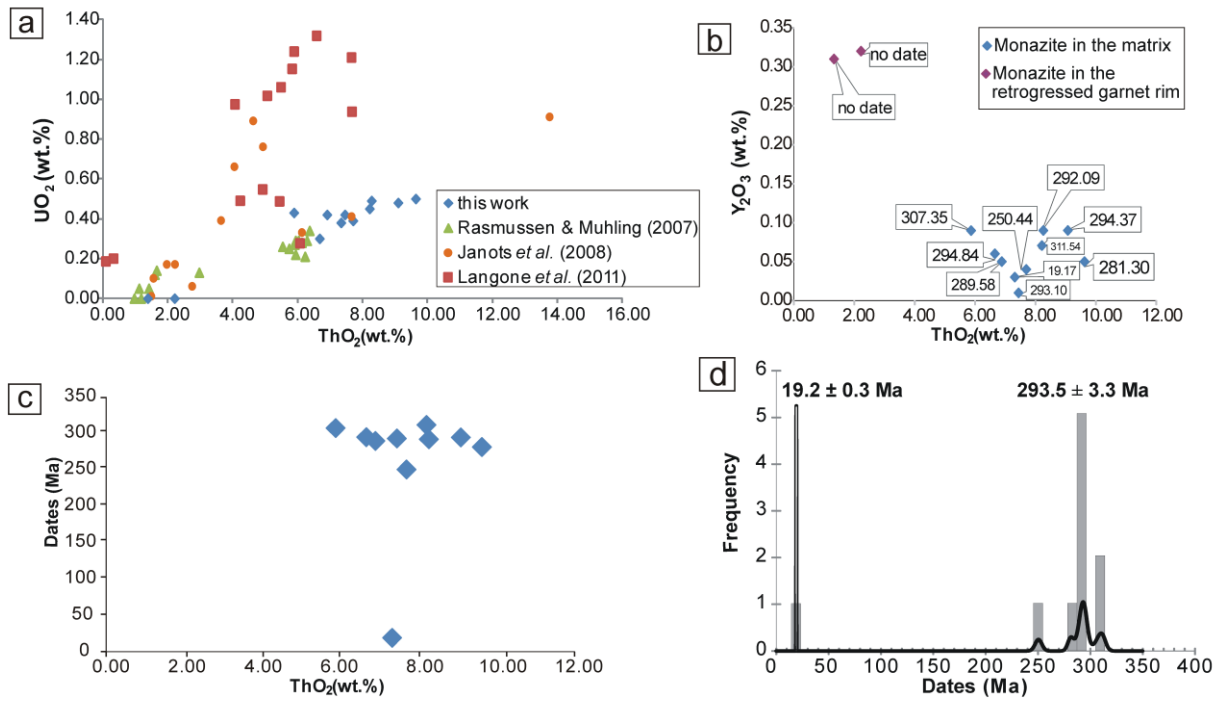


Microstructural site: retrogressed garnet rim

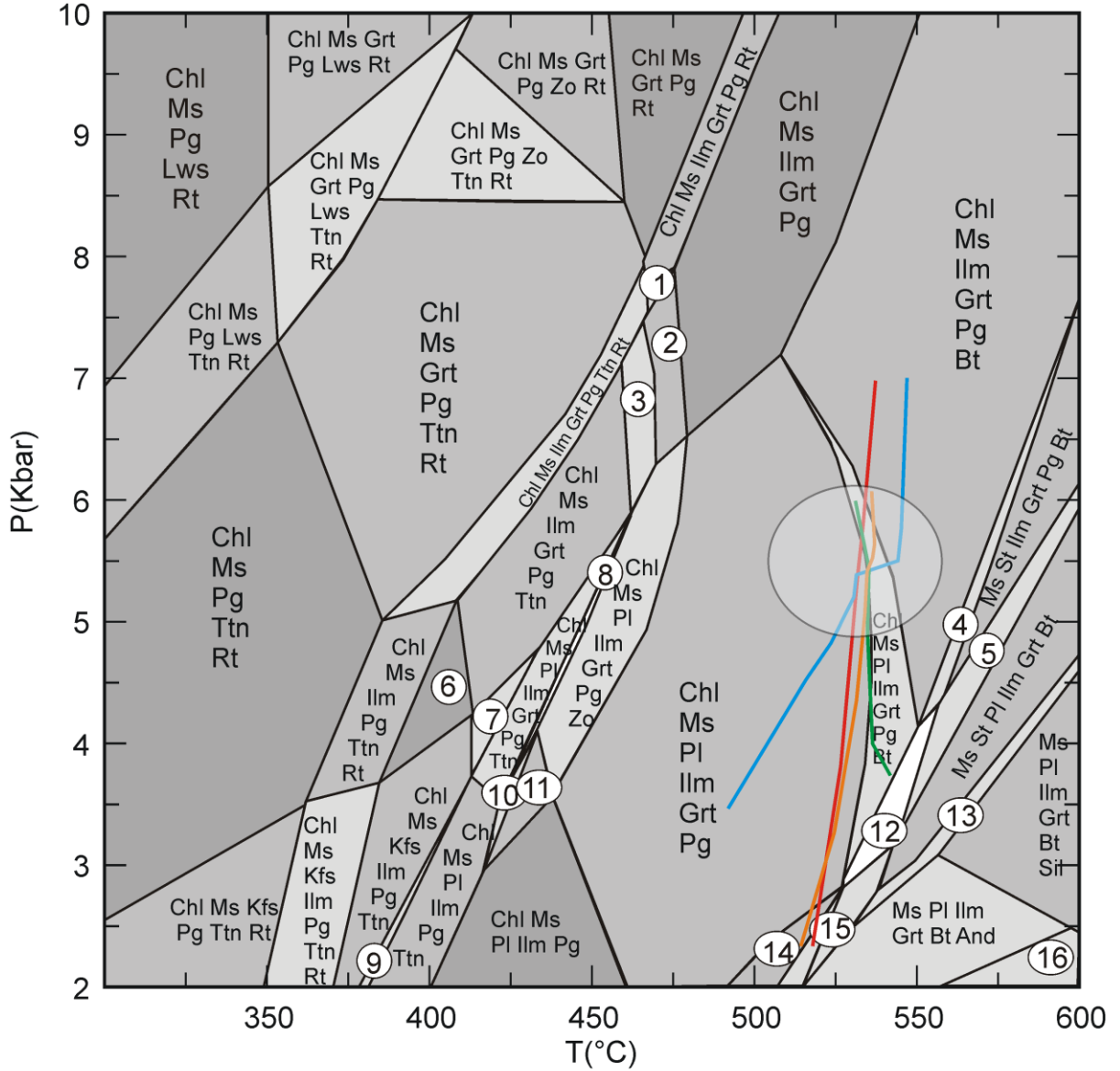




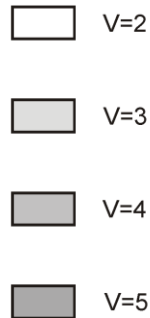




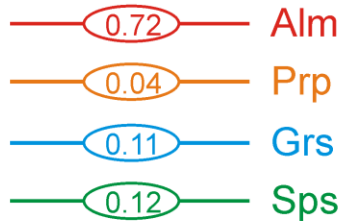
MnTiKCNFMASH (+ Qtz + H₂O)



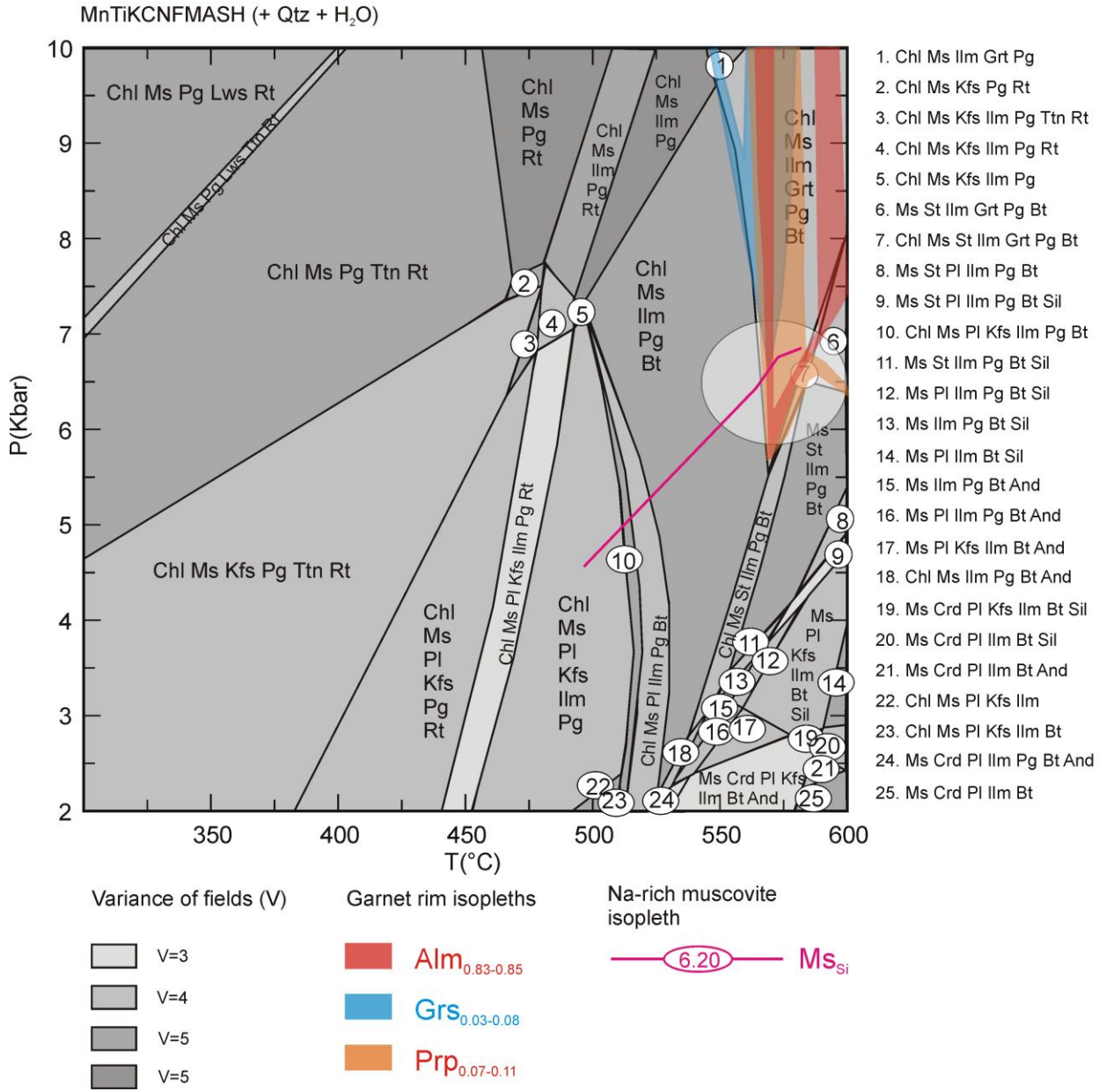
Variance of fields (V)

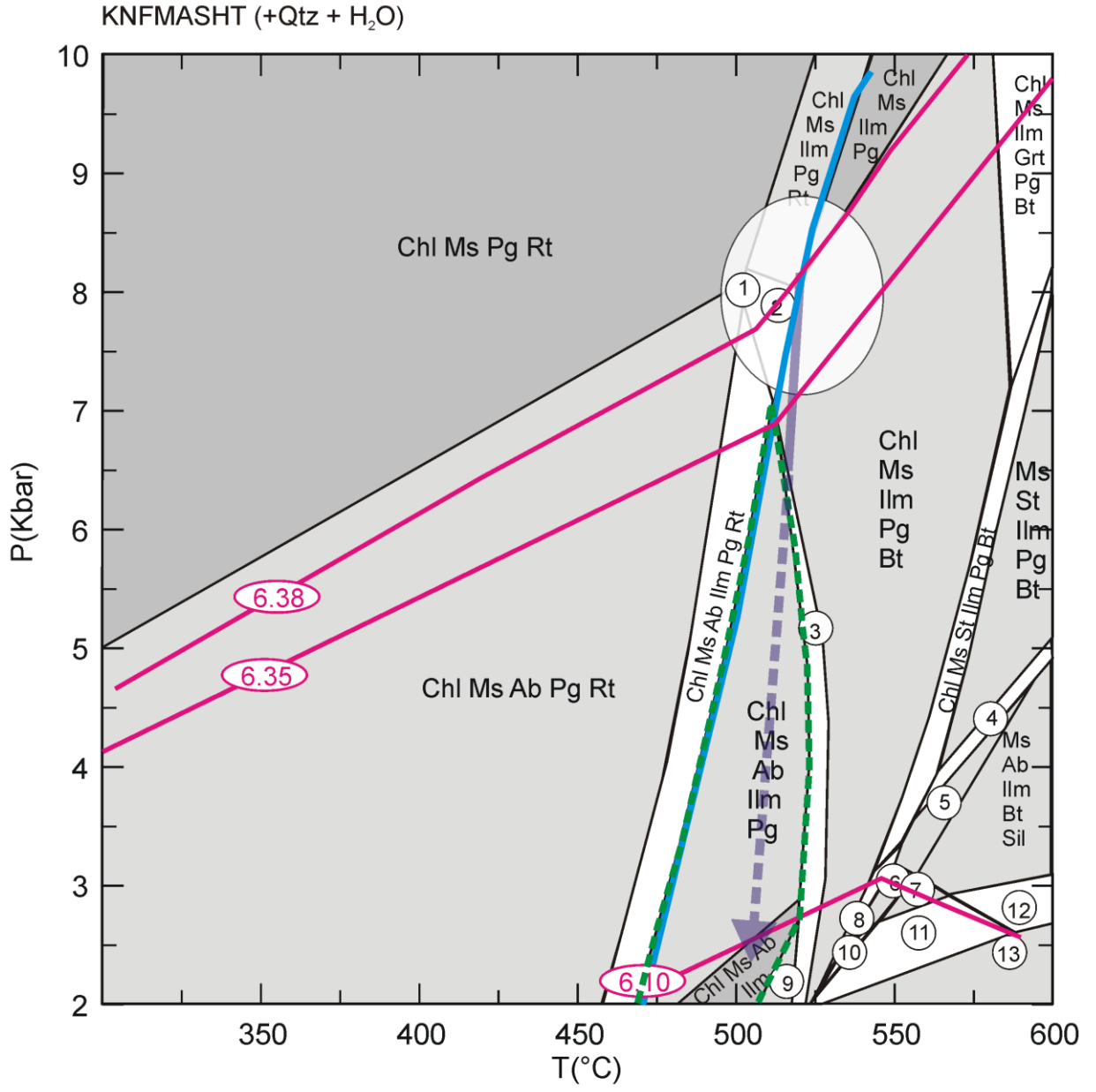


Garnet inner core isopleths



1. Chl Ms Ilm Grt Pg Zo Rt
2. Chl Ms Ilm Grt Pg Zo
3. Chl Ms Ilm Grt Pg Zo Ttn
4. Chl Ms St Ilm Grt Pg Bt
5. Ms St Pl Ilm Grt Pg Bt
6. Chl Ms Ilm Pg Ttn
7. Chl Ms Kfs Ilm Grt Pg Ttn
8. Chl Ms Pl Ilm Grt Pg Zo Ttn
9. Chl Ms Pl Kfs Ilm Pg Ttn
10. Chl Ms Pl Ilm Pg Zo Ttn
11. Chl Ms Pl Ilm Pg Zo
12. Chl Ms St Pl Ilm Grt Pg Bt
13. Ms St Pl Ilm Grt Bt Sil
14. Chl Ms Cld Pl Ilm Grt
15. Chl Ms Cld Pl Ilm Grt Bt
16. Ms Crd Pl Ilm Grt Bt And





Variance of fields (V)

□ V=2

□ V=3

□ V=4

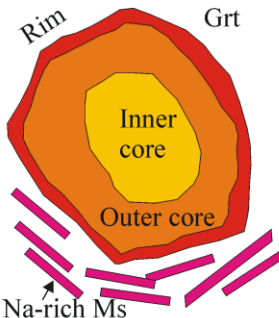
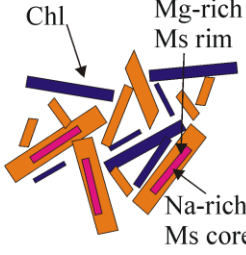
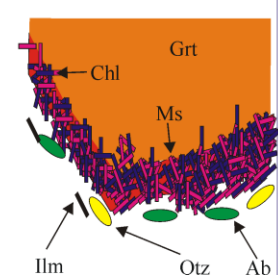
Isopleths

— 6.38 — Ms_{Si}

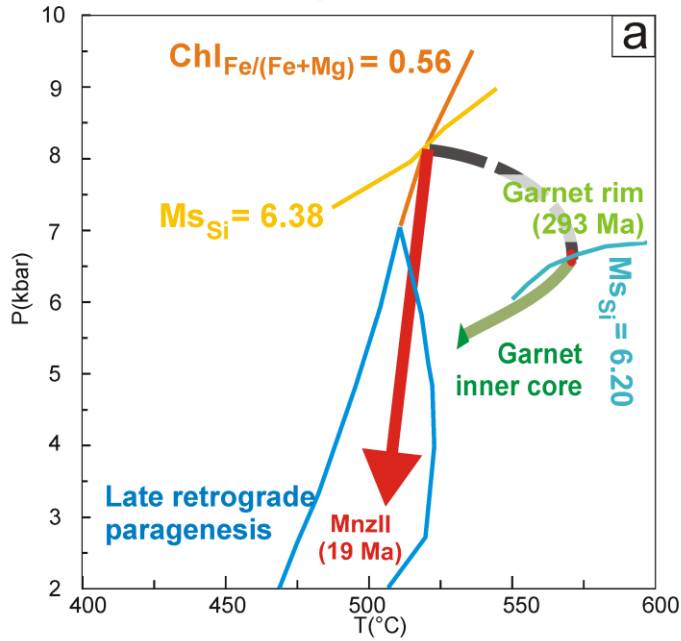
— 0.56 — Chl_{XFe}

— — — Retrograde paragenesis

1. Chl Ms Pg Bt Rt
2. Chl Ms Ilm Pg Bt Rt
3. Chl Ms Kfs Ilm Pg Bt
4. Ms St Ilm Pg Bt Sil
5. Ms Ilm Pg Bt Sil
6. Ms Ilm Pg Bt And
7. Ms Kfs Ilm Bt And
8. Chl Ms Ilm Pg Bt And
9. Chl Ms Kfs Ilm Bt
10. Ms Crd Ilm Pg Bt And
11. Ms Crd Kfs Ilm Bt And
12. Ms Crd Kfs Ilm Bt Sil
13. Ms Crd Kfs Ilm Bt

	PEAK TEMPERATURE STAGE		PEAK PRESSURE STAGE	RETROGRADE STAGE
MICROSTRUCTURES	 <p>Garnet porphyroblasts and Na-rich cores in potassic white mica</p>		 <p>Mg-rich rims around Na-rich-cores in potassic white mica and chlorite with decussate structure. Mg-rich potassic white mica occurs also in the recrystallized areas</p>	 <p>Late observed paragenesis</p>
CONSTRAINING PHASES	Garnet composition		Si max=6.28 in potassic white mica rims and XFe=0.56 in chlorite	Late paragenesis and low Si content in potassic white mica
	INNER CORE Alm ₇₂ Sps ₁₂ Grs ₁₁ Prp ₄	RIM Alm ₈₃₋₈₅ Grs ₃₋₈ Prp ₇₋₁₁		
COMPUTED ASSEMBLAGE	Si max in potassic white mica cores=6.20		Ms Chl Pg Ilm Qtz	Ms Chl Ab Ilm Qtz
	Ms Chl Pg Pl Ilm Grt Qtz	Ms Chl Pg Ilm Grt Bt Qtz		
OBSERVED ASSEMBLAGE	Ms Chl Pl Ilm Grt Qtz <i>Xen</i>	Ms Chl Ilm Grt Qtz <i>MnzI</i>	Ms Chl Ilm Qtz	Ms Chl Ab Ilm Qtz <i>MnzII, Ap, Alm, Ep</i>
T	530 °C	575 °C	520 °C	475-520 °C
P	5.5 kbar	7 kbar	8 kbar	2-7 kbar
Age		293 Ma		19 Ma

Monometamorphic anticlockwise P - T - t path



Polymetamorphic clockwise P - T - t paths

